Chapter 3

Chapter 3

Synthesis, Single Crystal X-ray, In Silico, and In Vitro Biological Evaluation of N-benzyl-4-(4-chlorophenyl)-2-oxobutanamide

3.1. Introduction

α-Ketoamide is a privileged motif as well as the key intermediate in medicinal, synthetic chemistry, and chemical biology. The chemistry of *α*-ketoamide has been discussed in **Chapter 1, Section 1.11**. *α*-Ketoamide derivatives have been reported as calpain, Caspase, Dengue virus protease, HIV-protease, and Gastric pancreatic lipase inhibitors possessing good metabolic and chemical stability in comparison to other aldehyde derivatives [1]. Taking the opportunities in this moiety, several dicarbonyl-containing molecules have been developed into well-known clinically used drugs such as Indibulin (anticancer), Biricodar (anticancer), Boceprevir (anti-HCV), etc. (**Figure 3.1**)[2].

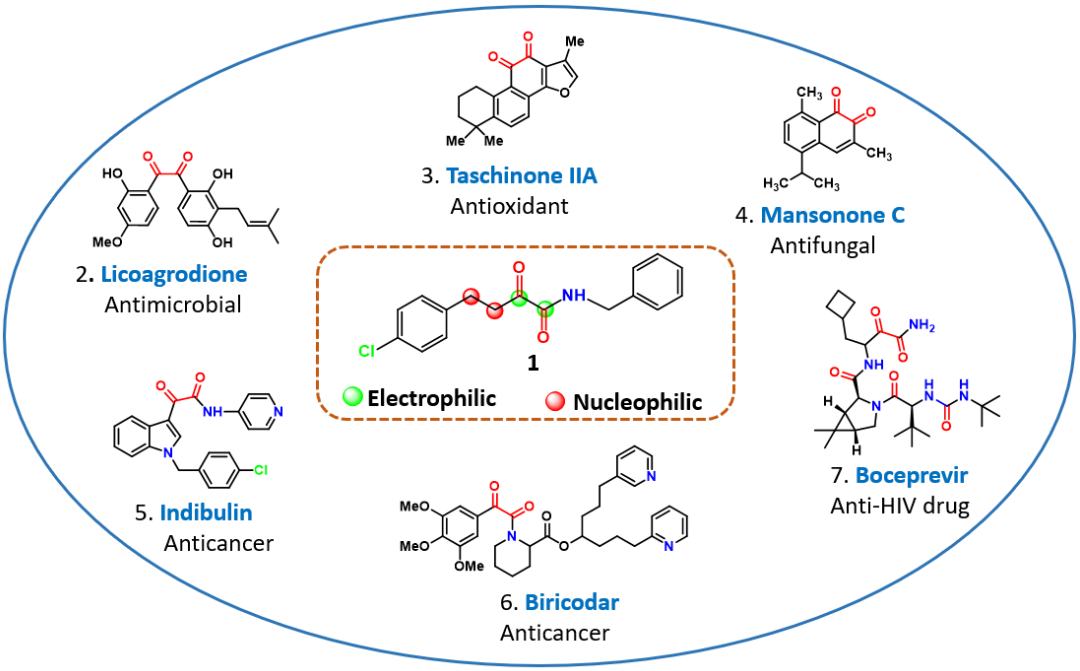

Figure 3.1. α-Ketoamides as a potential source of clinical drugs. Potential reaction sites in *α*-ketoamide (1). Dicarbonyl-containing natural products (compounds **2**, **3** & **4**). Dicarbonyl-containing drug molecules (compounds **5**, **6** & **7**).

A lot of interest has been garnered in the scientific community for the exploration of α-ketoamides for their potential role in the development of lead candidates against different biological targets owing to their role in hydrogen bonding with the active site amino acids, better pharmacokinetic profile, superior metabolic and chemical stability, and resistivity to proteolytic cleavage in comparison to other α-ketoacids as well as α-ketoesters [1, 3].

Several methods have been reported for the synthesis of α-ketoamides [4-6] and some recent methods have been discussed in the **Chapter 1, Section 1.11.4**. In contrary to the most of the synthetic methods where researchers have been using strong oxidizing agents and strong coupling reagents, Das et. al., reported a new synthetic route for the synthesis of α-ketoamides from β,γ-unsaturated α-keto thioester [7].

3.2. Objectives

The objectives of this study are as follows:

- **Compound synthesis and characterization:** To synthesize α-ketoamide compound 1 and determine its structural properties through NMR spectroscopy, Mass spectrometry, and single-crystal X-ray crystallography.
- **In silico studies**: To perform Molecular docking against Aβ peptide monomer and fibril structure followed by molecular dynamics simulation to evaluate the binding mode of the compound with the target and to utilize DFT calculations to analyze the electronic structure, stability, and reactivity of compound 1, including optimizing its stable structure and identifying reactive sites.
- **In vitro biological evaluation**: To investigate the potential of compound 1 as an Aβ aggregation modulator, assessing its inhibition of Aβ aggregation using ThT assay and assessment of cytotoxicity in cell lines using MTT assay.

3.3. Results and Discussions

3.3.1. Synthesis of *N*-benzyl-4-(4-chlorophenyl)-2-oxobutanamide (Compound1)

The starting material 4-chlorobenzylidene (ii) was synthesized from 4-chloro benzaldehyde by interacting with Wittig salt in presence of dry THF [8]. Then compound (ii) undergoes Swern oxidation in presence of dimethylsulfoxide (DMSO) & PPh3.HBr to produce β,γ-unsaturated α-keto-methyl thioesters (iii)[8], further, it is reduced chemoselectively by triethylhydrosilane in presence of acid catalyst boron trifluoride diethyl etherate (BF_3OEt_2) [9]). Compound **1** is synthesized by reacting 4-chloro- β,γ-unsaturated-*α*-hydroxy thioesters (iv, 1 eq.) with 5 equivalent of 4-chlorobenzylamine in dry toluene. After 10 to 15 minutes when the reaction was completed, brine solution was added and the organic layer was separated. Then the reaction mixture was separated through column chromatography using 100-200 mesh size silica (**Scheme 3.1)**.

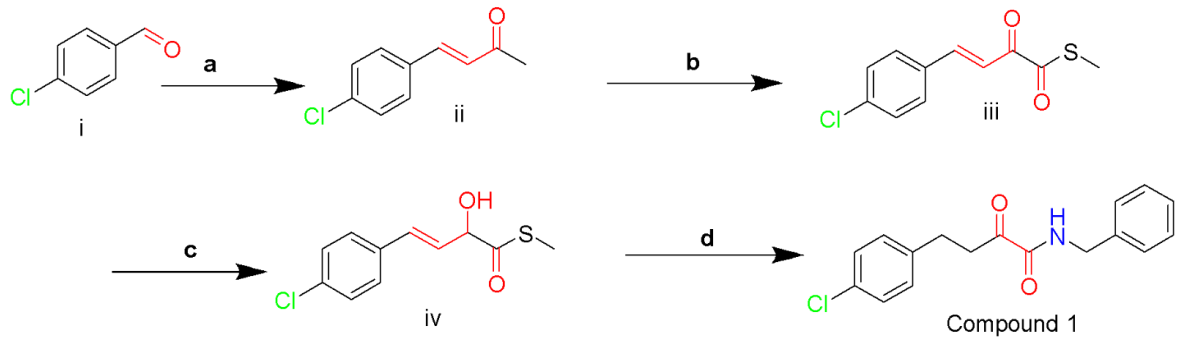

Scheme 3.1: Synthesis of compound 1. a. Wittig salt (1-(Triphenylphosphoranylidene)-2-propanone), THF, rt, **b.** PPh3.HBr, DMSO, 50 °C, **c.** Et_3SiH, BF_3OEt_2, Dry DCM, rt, **d.** benzylamine, toluene**,** rt.

Based on the previous reports the reaction is believed to proceed through the amine catalysed isomerization of allylic alcohol via intermediate I (Int-I) and intermediate (Int-II) which underwent amidation to yield the desired products. The mechanism for the synthesis of the compound **1** has been illustrated in **Figure 3.2.**

3.3.2. Description of The Crystal Structure

Single crystal X-ray diffraction analysis reveals that compound **1** crystallizes in monoclinic crystal system with space group $P2_1/c$ (No. 14) (**Table 3.1**). The asymmetric unit of compound **1** comprises of 21 crystallographically independent non-hydrogen atoms in which seventeen carbon atoms, one chlorine atom, one nitrogen atom, and two oxygen atoms are crystallographic independent (**Figure 3.3A**).

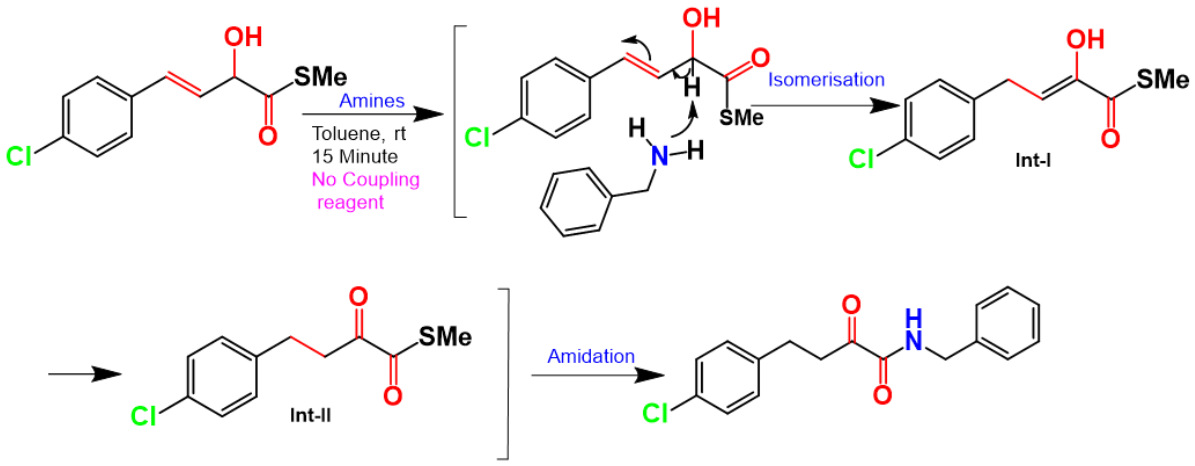

Figure 3.2. Schematic representation of mechanism of the synthesis of compound 1.

The asymmetric unit contains the complete fragment of compound **1.** The C–O, C–N, and C–Cl bond lengths are in the range of 1.200(3) *Å* to 1.735(2) *Å* (**ST 1**). The perspective ellipsoid view with a 50% probability is depicted in **Figure 3.3A**. The benzyl ring is almost perpendicular with respect to the other fragment along with chloro-benzyl ring in compound **1.** The overall packing is observed due to the alternative arrangement of full molecular unit maintaining the 2_1-screw axis of compound **1** (**Figure 3.3B**). Moreover, the overall three-dimensional structure can be stabilized through the intermolecular N—H••••O and C—H••••O hydrogen bonding interactions (**Figure 3.3C**).

Table 3.1: Crystal data and structure refinement parameters of compound 1.

Structural parameter	**Compound 1**
Empirical formula	$C_{17}H_{16}Cl_1N_1O_2$
Formula weight	301.76
T(K)	296
λ (M*o* Kα) (*Å*)	0.71073
Crystal system	Monoclinic
Space group	$P2_1/c$ (No. 14)
a (*Å*)	15.646(8)
b (*Å*)	10.344(5)
c (*Å*)	9.340(5)
β (deg.)	97.366(2)
V (*Å*)	1499.32(1)
Z	4
D (g cm^{-3})	1.337
μ (min^{-1})	0.258
F (000)	632
θ range (deg.)	2.366 to 24.994
Reflections collected	2573
Unique data	1920
R indexes [I > 2 σ (I)]	R_1 = 0.0520
	wR_2 = 0.1429
R indexes (all data)	R_1 = 0.0726
	wR_2 = 0.1537
GOF on F^2	1.063
CCDC No.	2196203
$\sum \lVert F_O \rvert - \lvert F_C \rVert / \sum \lvert F_O \rvert$. $wR_2 = \{\sum [w (F_O^2 - F_C^2)]/\sum [w (F_O^2)^2]\}^{1/2}$.	

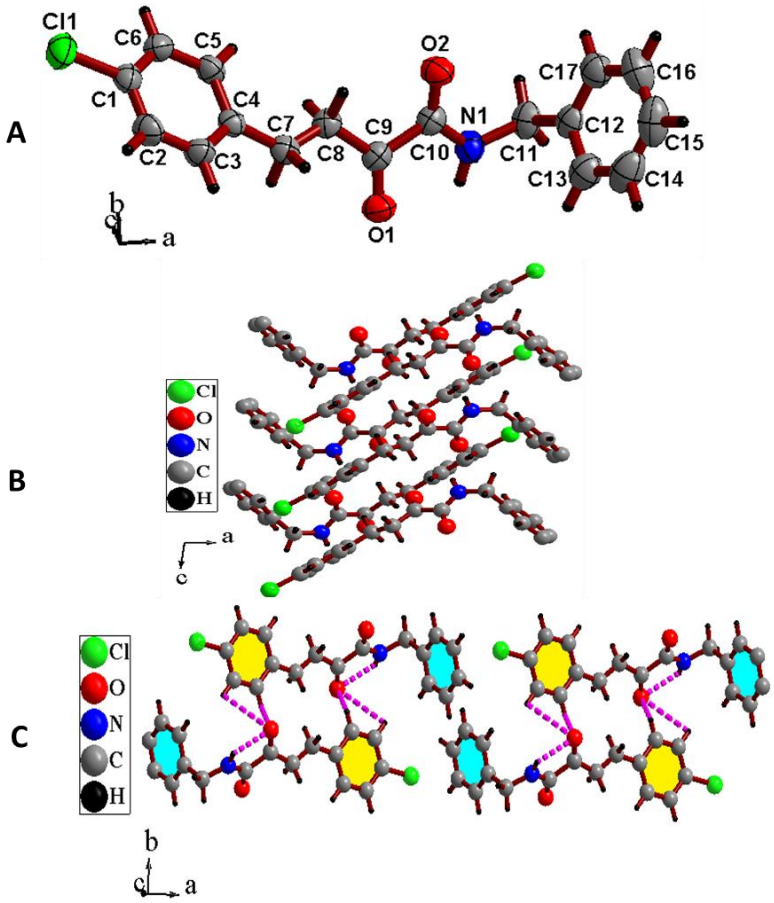

Figure 3.3. The asymmetric unit, overall packing structure, and intra- and intermolecular hydrogen bonding observed in the crystal structure of Compound 1. (A) The asymmetric unit of compound 1 with 50% probability displacement ellipsoid. (**B**) The overall packing structure of compound **1 in** *ac* plane, (**C**) The observed inter-molecular and intra-molecular hydrogen bonding interaction in the structure of compound **1**.

3.3.3. Hirshfeld Surface (HS) Analysis

Crystal Explorer version 21.5 software [8] was used to generate the molecule's Hirshfeld surfaces (HS) analysis and fingerprint plots (FPs). HS analysis is a quantitative way to study the detailed careful investigation of intermolecular interactions of the molecules in a crystal structure. Moreover, it gives detail of their crystal packing behaviour [9, 10]. The HS has been found as a region in crystal space around a molecule that is divided into two regions: the inner reference molecule and the outer neighbouring molecules. HS analyses has been performed in

order to visualize and evaluate the non-covalent interactions that assist to retain the crystal packing stability. All the qualities like d_{norm}, shape index, electrostatic potential and curvature were mapped to HS. The d_{norm} is knowns as normalized contact distance defined in the terms of external distance (de) and internal distances (di) and the van der Waals radii of atoms and it is expressed by: $d_{norm} = \frac{d_i - r_i^{vdW}}{r_i^{vdW}} + \frac{d_e - r_e^{vdW}}{r_e^{vdW}}$, where r_i^{vdW} and r_e^{vdW} are the van der Waals (vdW) radii of significant atoms internal and external to the surface, respectively [8, 11].

The white coloured regions represent the van der Waals contacts whereas the red and blue coloured regions constitute shorter and longer inter contacts, respectively. Short intermolecular interactions are seen as red patches in d_{norm} mapped on the HS (**Figure 3.4**).

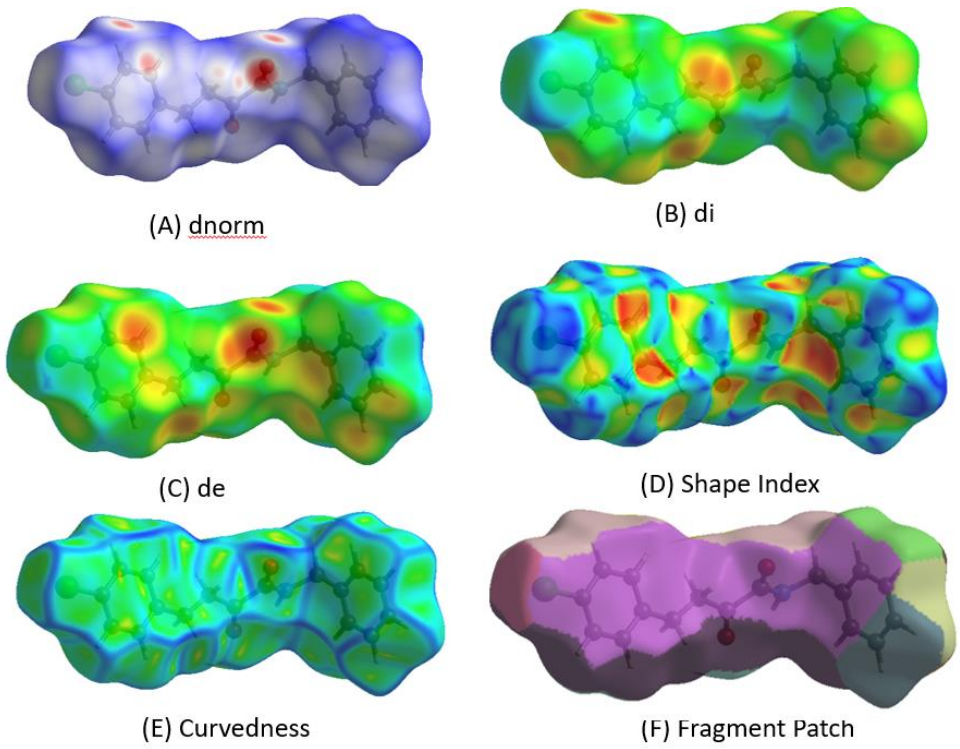

Figure 3.4. Hirshfeld surface analysis of the compound 1, mapped with d_{norm}(A), di (B), de (C), shape index (D) curvedness (E), Fragment patch (F).

The round type red coloured regions constitute the hydrogen bond interactions with neighbouring molecules according to the d_{norm}. Shorter contacts and longer contacts indicated

in red and blue represents the negative d_{norm} and positive d_{norm} value respectively. When intermolecular contacts are shorter than the vdW radii it is called shorter contacts and when intermolecular contacts are longer than the vdW radii it is called longer contacts. Similarly, the white region represents zero d_{norm} value (the contacts with distances are equal to the sum of the vdW radii). The fingerprint plots have been used to identify and compare various types of interactions.

The overall fingerprint plot for the compound **1** and relative contacts including H•••C/C•••H, H•••H, H•••N/N•••H, and Cl•••H/H•••Cl to the HS, are shown in **Figure 3.5**. The most common form of contact for compound **1** corresponds to H•••H interactions, which account for more than 40% all surface contacts. The existence of Cl—H/H-Cl contacts results in a pair of distinctive wings in the fingerprint plot, which is deconstructed into C•••H/H•••C surface contacts, which accounts for 21 % of the HS. Short O•••H/H•••O contacts provided a pair of spikes that accounts for 17.8 % of HS. N-H/H-N contacts, which account for 0.8 % of the entire surface, are represented as widely spread wings in **Figure 3.5**. Fingerprint percentage of the total surface area for closed contact between atoms inside and outside the surface for the compound 1 was mentioned in the **Table 3.2** and **Table 3.3**.

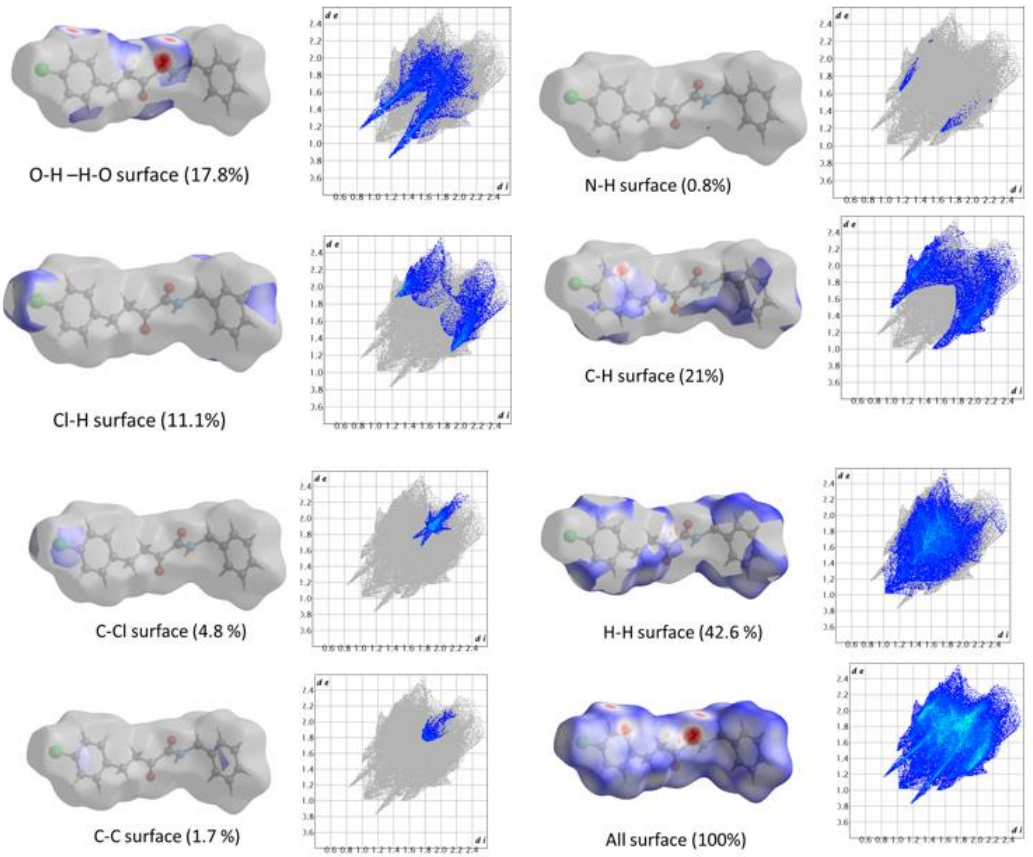

Figure 3.5. 2-D fingerprint plot of different contributions for the compound 1.

Table 3.2. Fingerprint percentage of the total surface area for closed contact (Included Reciprocal Contact) between atoms inside and outside the surface for compound 1.

Atoms	**Cl**	**O**	**N**	C	H
	Surface %				
C	4.8	0.2	0.0	1.7	21.1
Cl	0.0	0.0	0.0	4.8	11.1
H	11.1	17.8	0.8	21.1	42.6
N	0.0	0.0	0.0	0.0	0.8
O	0.0	0.0	0.0	0.2	17.8

Table 3.3. Fingerprint percentage of the total surface area for closed contact between atoms inside and outside the surface for the compound 1.

Mode	Minimum interaction	Mean interaction	Maximum interaction
di	0.849	1.705	2.568
de	0.848	1.709	2.619
D norm	-0.440	0.477	1.236
Shape index	-0.997	0.245	0.999
Curvedness	-3.766	-0.988	0.341

3.3.4. Energy Framework Calculations

Crystal Explorer 21.5 software, was used to determine the energy framework and interaction energies of the compound **1** (**Figure 3.6**)[12]. By using the B3LYP/6–311 G(d, p) energy model in Crystal Explorer with scale factors *k_ele* = 1.019, *k_pol* = 0.651, *k_disp* = 0.901, and *k_rep* = 0.811, correspondingly, the intermolecular interaction energies for the compound 1 were calculated.

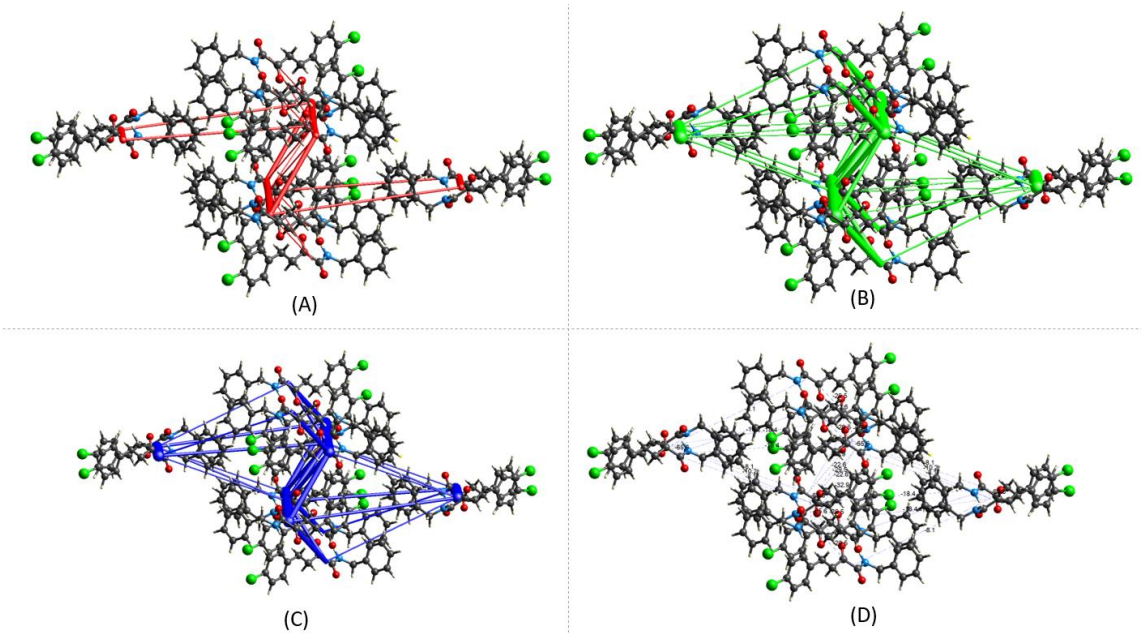

Figure 3.6. Different Energy Frameworks for interaction. (**A**) coulomb energy, (**B**) dispersion energy (**C**) total energy, (**D**) total energy annotated of compound **1**, the cylindrical

radius is proportional to the relative strength of the corresponding energy.

Table 3.4 lists the result of different interaction energies of the compound 1, the calculated electrostatic, polarization, dispersion, and repulsion energies are −82 *kJ mol*$^{-1}$, −19.7 *kJ mol*$^{-1}$, −207.8 *kJ mol*$^{-1}$ and 140.6 *kJ mol*$^{-1}$, respectively. The calculated total energy of the compound 1 is −195.4 *kJ mol*$^{-1}$. The results constitute that dispersion and repulsion energy are leading over other interaction energies and have a key role in the total forces in the crystal packing. For better comprehension, we have shown the obtained energy framework analysis data in **Table 3.5.**

Table 3.4. Different interaction energies of the compound 1 in *kJ mol*$^{-1}$.

Energy Model	***k_ele***	***k_pol***	***k_disp***	***k_rep***
B3LYP/6-31G(d,p)electron densities	1.057	0.740	0.871	0.618
B3LYP/6-31G(d,p)	-82	-19.7	-207.8	140.6

Table 3.5 Interaction energy (kJ/mol), N = number of atoms, R is the distance between molecular centroids (mean atomic position) in Å. Total energy, only reported for two benchmarked energy model, are the sum of the four energy components, scaled appropriately.

Sl No	***N***	**Symop**	***R***	**Electron density**	***E_ele***	***E_pol***	***E_dis***	***E_rep***	***E_total***
1	2	x, -y+1/2, z+1/2	16.90	B3LYP/6-31G(d,p)	-11.7	-0.2	-6.7	0.0	-18.4
2	2	x, -y+1/2, z+1/2	4.69	B3LYP/6-31G(d,p)	-34.9	-9.4	-77.0	73.4	-65.6
3	2	-x, y+1/2, -z+1/2	6.08	B3LYP/6-31G(d,p)	-6.8	-2.3	-27.6	16.6	-22.6
4	1	-x, -y, -z	5.68	B3LYP/6-31G(d,p)	-4.9	-1.5	-43.2	23.3	-29.5
5	2	x, y, z	15.65	B3LYP/6-31G(d,p)	0.8	-0.3	-6.3	0.0	-5.0
6	1	-x, -y, -z	14.19	B3LYP/6-31G(d,p)	-0.4	-0.3	-10.9	0.0	-10.2

7	2	-x, y+1/2, -z+1/2	15.00	B3LYP/6-31G(d,p)	0.0	-0.2	-9.2	0.0	-8.1
	1	-x, -y, -z	6.43	B3LYP/6-31G(d,p)	-23.7	-5.4	-23.8	27.3	-32.9
8									
9	1	-x, -y, -z	14.51	B3LYP/6-31G(d,p)	-0.4	-0.1	-3.1	0.0	-3.1

3.3.5. Optimization of the Geometry

The geometrically optimized three-dimensional conformation of the compound obtained by using the DFT calculation with the help of B3LYP/6-311G (d, p), basis set along with their atomic labelling is represented in **Figure 3.7**. There is a total of 37 atoms in the compound 1. The bond length and bond angles calculated from DFT were further matched with the experimental results represented in **Table 3.6**. This determines the robustness of the theoretical calculation result obtained from the DFT/B3LYP using the 6311G (d, p) basis set, as it is evident that all the C=O bond lengths are about 1.2 *Å* and C-Cl bond length is around 1.7 *Å*. Thus, it can be further used for predicting such analogous compounds.

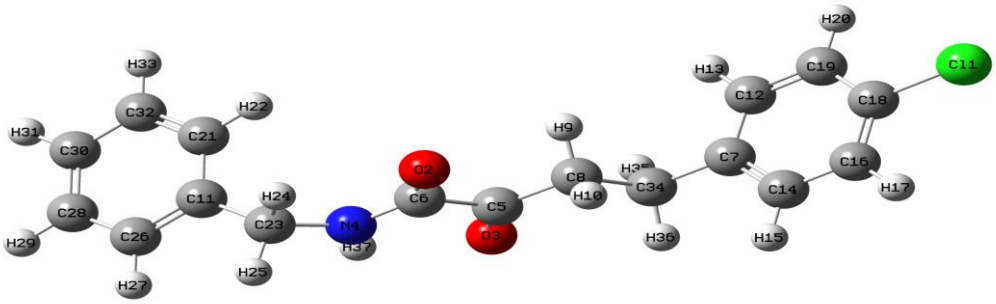

Figure 3.7. Optimized molecular structure obtained by DFT method of the compound 1.

Table 3.6. Optimized geometrical parameters (Bond Length (*Å*) and Bond Angle (º).

Parameter	B3LYP/6-311G(d, p)	Experimental	Parameter	B3LYP/6-311G(d, p)	Experimental
	Bond length (Å)	Bond length (Å)		Bond angle (º)	Bond angle (º)
C(36)-H(37)	1.0845	1.07	H(37)-C(36)-C(34)	120.0713	106.9999
C(34)-C(36)	1.3951	1.3572	H(37)-C(36)-C(28)	120.1899	106.3861
C(34)-H(35)	1.085	1.3506	C(34)-C(36)-C(28)	119.7385	120.3265
C(30)-H(32)	1.0934	1.07	C(36)-C(34)-H(35)	120.0283	106.2955
C(30)-H(31)	1.0935	1.384	C(36)-C(34)-C(21)	120.2326	107.1194
C(28)-C(36)	1.3914	0.8914	H(35)-C(34)-C(21)	119.738	120.2684
C(28)-H(29)	1.084	0.9701	H(20)-C(19)-C(18)	120.1191	106.1417
C(26)-C(28)	1.3949	0.9703	H(20)-C(19)-C(12)	120.8201	105.7318
C(26)-H(27)	1.0857	1.43	C(18)-C(19)-C(12)	119.0604	105.7605
C(23)-H(25)	1.0931	1.4642	C(19)-C(18)-C(16)	120.9802	105.7608
C(23)-H(24)	1.0909	0.93	C(19)-C(18)-Cl(1)	119.516	105.7599
C(21)-C(34)	1.3907	1.3808	C(16)-C(18)-Cl(1)	119.503	126.2727
C(21)-H(22)	1.0846	0.9298	C(18)-C(16)-H(17)	120.0971	119.9356
C(19)-H(20)	1.0824	1.3809	C(18)-C(16)-C(14)	119.0604	119.8712
C(18)-C(19)	1.3901	0.9696	H(17)-C(16)-C(14)	120.842	120.1931
C(16)-C(18)	1.3899	0.9696	C(16)-C(14)-H(15)	118.9649	119.5428
C(16)-H(17)	1.0824	1.4981	C(16)-C(14)-C(7)	121.4296	119.5022
C(14)-C(16)	1.3922	1.4724	H(15)-C(14)-C(7)	119.6042	120.955
C(14)-H(15)	1.0855	0.9301	C(19)-C(12)-H(13)	118.9505	107.8808
C(12)-C(19)	1.3923	1.3856	C(19)-C(12)-C(7)	121.4392	109.0605
C(12)-H(13)	1.0858	0.9301	H(13)-C(12)-C(7)	119.6089	109.0635
C(11)-C(26)	1.3957	1.3746	C(30)-C(7)-C(14)	120.9671	109.0451
C(11)-C(23)	1.517	1.3798	C(30)-C(7)-C(12)	120.9914	109.0491
C(11)-C(21)	1.4003	1.3795	C(14)-C(7)-C(12)	118.0297	112.6299
C(8)-C(30)	1.5342	1.7353	H(32)-C(30)-H(31)	106.0207	119.7718
C(8)-H(10)	1.0963	0.9302	H(32)-C(30)-C(8)	109.057	119.7797
C(8)-H(9)	1.096	1.3831	H(32)-C(30)-C(7)	110.0442	120.4481
C(7)-C(30)	1.5113	0.9301	H(31)-C(30)-C(8)	109.0173	120.3692
C(7)-C(14)	1.3986	1.3894	H(31)-C(30)-C(7)	110.0417	120.4521
C(7)-C(12)	1.398	0.9303	C(8)-C(30)-C(7)	112.4477	119.1786
C(5)-C(8)	1.5075	1.4004	C(36)-C(28)-H(29)	120.1151	119.4675
C(5)-C(6)	1.5512	0.9702	C(36)-C(28)-C(26)	119.9734	119.4948
N(4)-H(33)	1.0121	0.9704	H(29)-C(28)-C(26)	119.9114	121.0343
N(4)-C(23)	1.4602	1.4662	C(28)-C(26)-H(27)	119.6838	120.2012
N(4)-C(6)	1.3495	1.2229	C(28)-C(26)-C(11)	120.676	120.2426
O(3)-C(5)	1.2113	1.42	H(27)-C(26)-C(11)	119.6394	119.5562
O(2)-C(6)	1.2219	1.5428	C(34)-C(21)-H(22)	120.2791	119.5612
Cl(1)-C(18)	1.7609	1.1991	C(34)-C(21)-C(11)	120.4148	119.5741
			H(22)-C(21)-C(11)	119.3058	120.8648

C(26)-C(11)-C(23)	120.8376	119.3822
C(26)-C(11)-C(21)	118.9645	119.3759
C(23)-C(11)-C(21)	120.1953	121.2419
H(25)-C(23)-H(24)	108.1481	122.1451
H(25)-C(23)-C(11)	110.0794	120.0634
H(25)-C(23)-N(4)	108.5065	117.7727
H(24)-C(23)-C(11)	110.447	106.8804
H(24)-C(23)-N(4)	106.2459	107.3643
C(11)-C(23)-N(4)	113.2233	107.3492
C(30)-C(8)-H(10)	111.6966	107.3743
C(30)-C(8)-H(9)	111.7766	107.3541
C(30)-C(8)-C(5)	113.3709	119.8774
H(10)-C(8)-H(9)	103.9369	123.1978
H(10)-C(8)-C(5)	107.6996	118.7016
H(9)-C(8)-C(5)	107.8238	118.0897
C(8)-C(5)-C(6)	115.648	120.5658
C(8)-C(5)-O(3)	124.196	124.4147
C(6)-C(5)-O(3)	120.1554	114.955
C(5)-C(6)-N(4)	112.4378	119.4925
C(5)-C(6)-O(2)	121.291	125.5143
N(4)-C(6)-O(2)	126.2702	114.9812
H(33)-N(4)-C(23)	120.3421	118.7661
H(33)-N(4)-C(6)	116.0247	119.6233
C(23)-N(4)-C(6)	123.2826	121.474

3.3.6. Vibrational Spectra Calculation

The vibrational frequencies have been calculated for the compound having 37 atoms and 105 modes (3n-6) with the help of B3LYP 6311g (d, p) basis set which consists of stretching modes, bending modes, CH modes, torsion modes and out of plane modes. **Figure 3.8** shows the comparison of predicted IR spectra vs the experimental FT-IR spectra of the compound **1**. The experimental and theoretically computed frequencies can see to be evidently consistent, showing that the theoretical studies were well in accordance with the experimental results. The obtained IR intensities helped to characterize and identify the basic modes more precisely. Here, only the characteristic stretching vibration bands were seen. The important vibrations along with their characteristics like intensities are explained below.

N-H bond stretching vibrations of secondary amide are expected in between 3170-3370 cm^{-1},

which is the typical region for quick detection of secondary amine group systems [13, 14]. Because secondary amides contain one N-H bond, there is only one N-H stretching peak, seen at 3298.15 for compound **1** in **Figure 3.8**. The presence of C-H stretching vibrations in the aromatic structure is seen in the range 3110-3000 cm^{-1}, which is the typical region for the quick detection of C-H stretching vibrations. C-H stretching vibrations were found by in the range 3100-3000 cm^{-1} for asymmetric stretching vibrations and 2990-2850 cm^{-1} for symmetric stretching vibrations [15]. Experimentally, C-H stretching vibrations the FT-IR bands for compound 1 were observed at 3028.01, 2921.81and 3124 cm^{-1} as pure modes. In the region 1500–1000 cm^{-1}, the C–H in-plane bending vibrations are observed as strong to weak intensity bands. H– C–H in-plane bending vibrations of the compound are observed at 1488, 1452, 1451, 1391, 1365 cm^{-1} experimentally. The (C=C) ring stretching vibrations anticipated within the range 1300–1000 cm^{-1}. In the compound 1, the theoretical wavenumbers assigned to C–C stretching vibrations are 1524, 1488, 1452, 1391, 1365, 1288, 1245, 1222, and 1108 cm^{-1}. All C=C and C-C bands fall in the suitable region. Substituent brings little variations in the C=C stretching vibrations.

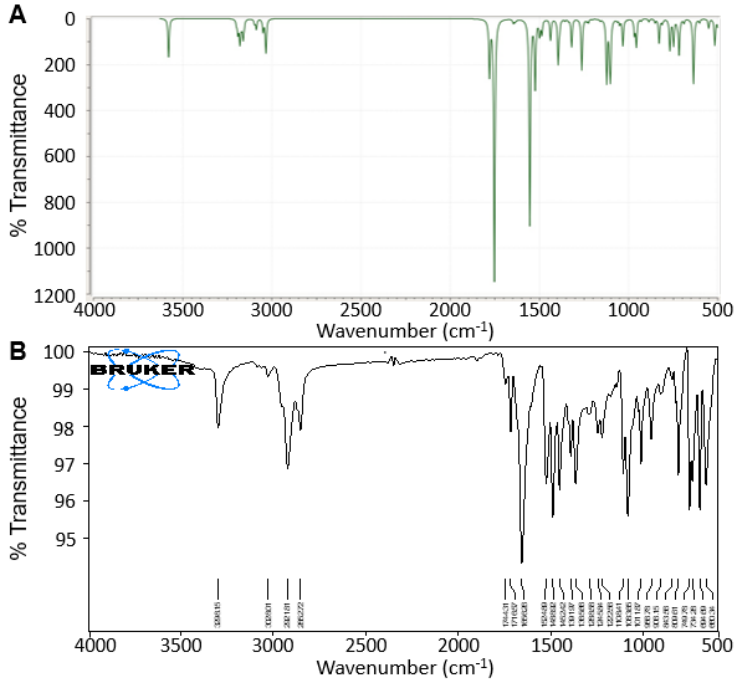

Figure 3.8. (A) Experimental and (B) Theoretical FT-IR spectra of compound 1.

The C=O stretch of the secondary amide is seen in **Figure 3.8** at 1656. 26, in the 1680 to 1630 range typical of all amides [16]. Carbonyl (C=O) stretching vibrations in ketones appears at approximately 1700 cm^{-1} [17]. Very strong bands in the FT-IR for C=O stretching vibrations of compound 1 were observed at 1716.57, 1744.37 cm^{-1} experimentally and theoretically from DFT calculation were observed at 1751.6 and 1779.26 cm^{-1} respectively.

3.3.7. Molecular Electrostatic Potential

Molecular electrostatic potential (MEP) was evaluated for the optimized geometry with an objective to understand the electrophilic and nucleophilic attack sites available in the compound 1. It is a pictorial representation of the electrostatic density in the 3D structural position around the molecule which can help to predict the sites for nucleophilic and electrophilic processes that might occur. Represented with definite colour maps as red < orange < yellow < green < blue. The red regions are indicative of negative electrostatic potential having the highest repulsion whereas the positive electrostatic regions are denoted by blue region having the strongest attraction whereas the green region is for the neutral potential. The regions having the concentrated negative potential in the molecule were identified, the red dots surrounding the O2 and O3 atom on the compound in the MEP map shows the electrophilic reactivity, whereas the region around N4 and the region around the carbon atoms represents the nucleophilic reactivity as denoted by the blue colour in the MEP map (**Figure 3.9**.).

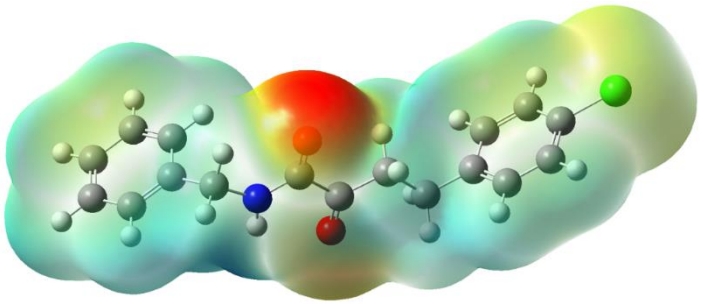

Figure 3.9. Molecular Electrostatic Potential (MEP) of compound 1.

3.3.8. UV-Vis Spectroscopy

In order to obtain the absorbance spectra of the compound **1,** the UV-Vis spectroscopic measurement was carried out at room temperature using methanol as a solvent. Also, the UV-Vis spectrum was theoretically calculated in gas phase and methanol using TD-DFT method utilizing B3LYP/6-311G (d, p) basis set and selecting the CPCM solvent model (**Figure 3.10**). It can be seen from the TD-DFT calculated spectra that it estimates a strong electronic transition for the compound at 280 *nm* in the gas phase and 282 nm in methanol. The experimental λ_{max} was found to be around 217.9 *nm* using methanol as a solvent.

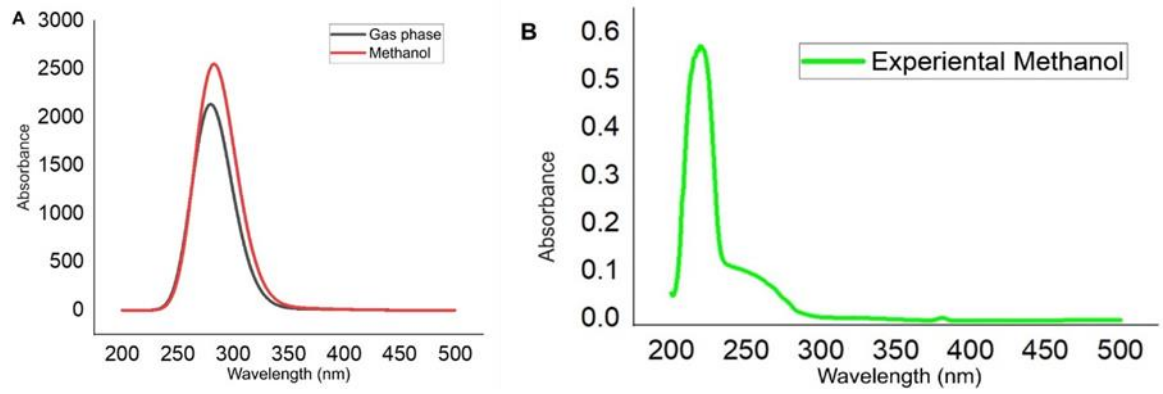

Figure 3.10. Theoretical (A) and experimental (B) UV-Vis spectra of compound 1.

3.3.9. HOMO-LUMO Analysis and Reactivity Descriptors

The Frontier molecular orbitals (FMOs) are the most crucial orbitals present in the molecule that helps in the better understanding of the electronic, thermal, and chemical characteristics, known as the highest occupied molecular orbital (HOMO) and lowest unoccupied molecular orbital (LUMO) [18, 19]. The study of HOMO-LUMO energy gap is the best-suited parameter for the estimation of the reactivity in quantum chemistry. The generic ability of the charge transfer interaction within the molecule where HOMO has a higher propensity to give the electrons, likewise the LUMO has a higher propensity to gain the electrons and thus can be studied in order to predict the charge transfer. The HOMO and LUMO plot along with their energy values for the compound 1 is shown in **Figure 3.11** with the help of DFT/B3LYP

method using the 6-311G (d, p) basis set in the gas phase and various parameters of the calculation like HOMO-LUMO energies, ionization potential, electron affinity, energy gap, electronegativity, chemical potential, chemical hardness, chemical softness, and electrophilicity index are given in **Table 3.7**.

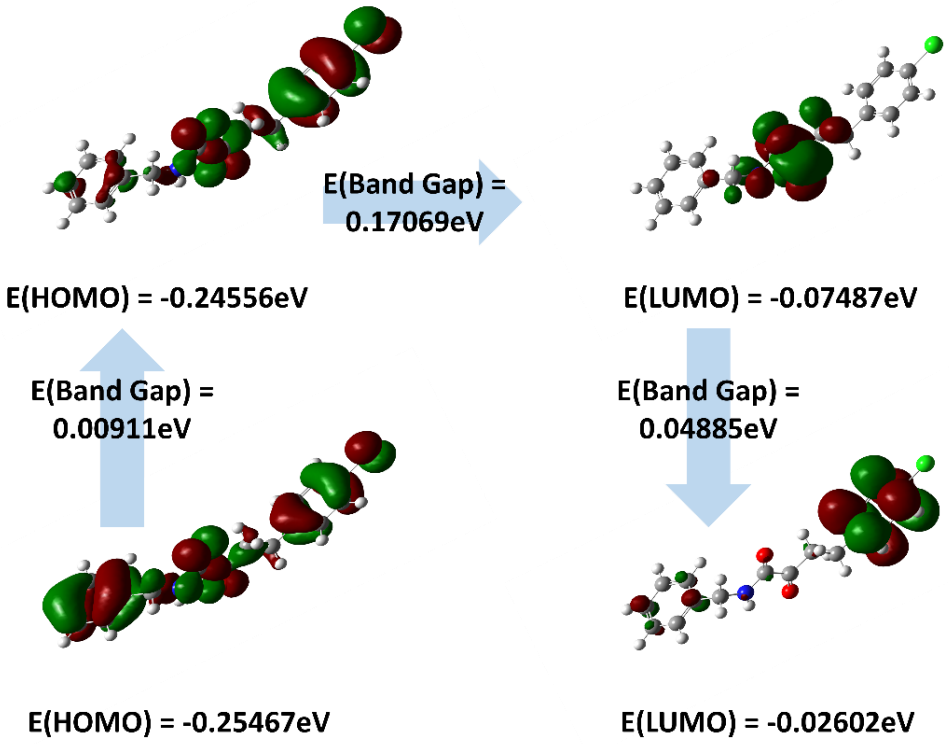

Figure 3.11. HOMO LUMO diagram of compound 1.

The HOMO-LUMO energy was evaluated with correspondence to the literature where the HOMO-LUMO energy difference can help to elementarily denote the chemical reactivity of the compound, where the big energy band gap in the HOMO-LUMO suggests greater stability as well as low chemical reactivity because of its energetically unfavourable nature to add an electron to the LUMO in order to extract an electron from the HOMO. The compound appears to be more reactive (E= E_{HOMO}-E_{LUMO} =0.17069 *eV*) based on the data obtained. Additionally, the HOMO seems to be localized around the chloro benzyl ring, whereas the LUMO cloud on the other hand seems to be centered over the ketoamide group. It has been reported in the literature that the compounds having a stabilized LUMO energy display excellent biological

activity. This might be due to the presence of carbonyl group that acts as an electron withdrawing agent [20].

Other parameters along with LUMO energy are all considered for the display of excellent biological activity like the global chemical reactivity descriptors given in **Table 3.7** which have been reported to be in agreement with the framework of Koopmans theorem. The reactive nature of the atoms and molecules are determined by their ionization potential. Stability and reactivity can be predicted from their absolute hardness and softness where it is evident that hard molecules tend to have a big energy gap and on the other hand soft molecules seems to have a small energy gap.

Table 3.7. Global and local reactivity descriptors for the compound 1.

Parameters	Value(*eV*)
E_{HOMO}	-0.24556
E_{LUMO}	-0.07487
Ionization potential	0.24556
Electron affinity	0.07487
Energy gap (E)	-0.17069
Electronegativity	0.160215
Chemical potential	-0.160215
Chemical hardness	0.085345
Chemical softness	5.858574
Electrophilicity index	0.1503828

3.3.10. Mulliken Population Analysis and Fukui Function

Mulliken population analysis (MPA) has been carried out using the B3LYP/6-311G (d, p) basis set employing DFT in order to predict the Fukui function and their individual atomic charges. It predicts the atoms in a molecule that has a high propensity to lose or absorb electrons [21, 22]. As showed in the **Figure 3.12**, the hydrogen atoms seem to be positively charged. Mulliken atomic charge showed that Cl1 exhibits a negative charge, and the atomic charges for the nitrogen and oxygen atoms are found to be negative. The dual descriptor ($\Delta f(r)$) differentiates the electrophilic and nucleophilic Fukui functions and it can be expressed by equation 1 [23].

$$\Delta f(r) = [f^{+}(r) - f^{-}(r)] \text{ ……... eq. 1}$$

The nucleophilic sites in the compound 1 are C5, C6, C16, and C19 (+ve value, Δf(r) > 0). Cl1, O2, O3, N4, C7, C8, C11, C12, C14, C18, C21, O23, C26, C28, C30, C32, and C34 (-ve value i.e. Δf(r) < 0) are electrophilic sites. The observed Δf(r) value revealed that compound **1** has more electrophilic sites which demonstrate its reactivity of the compound 1 in the biological system.

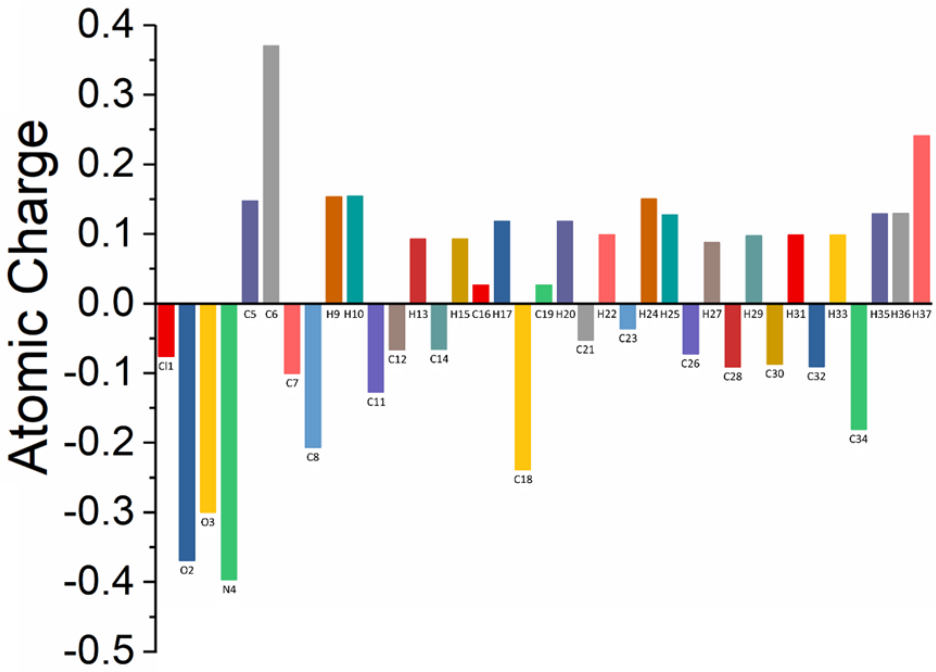

Figure 3.12. Graph showing Mulliken Population charges for the compound 1.

3.3.11. NBO and NHO Analysis

Natural bond orbital (NBO) analysis helps in understanding the interactions in both the filled and virtual spaces that can potentially enhance the intra- and intermolecular interaction analysis [19, 24]. The calculation was carried out at the same level of theory**. Table 3.8** shows the electron in the core, valence, and Rydberg subshells of the molecule. The percentage contribution for the natural population analysis and natural Lewis structures of the compound 1 is shown in **Figure 3.13**. This gives a detailed analysis elucidating various intramolecular and intermolecular interactions that may weaken the bond associated with the anti-bonding orbital

of the molecule. Thereby calculates the second-order perturbative estimates of the bonding anti-bonding interface in an NBO basis resulting in the loss of occupancy from the localized NBOs of the idealized Lewis structure to non-Lewis vacant orbitals. E(2) represents the stabilization energy associated with the delocalization of electron which is calculated for each of the donor NBO (i) and acceptor NBO (j). **Table 3.8** summarizes the second-order perturbation theory study of the Fock matrix in an NBO basis.

NBO analysis was carried out using the B3LYP method and the 6-311G (d, p) basis set on the compound 1 to unfold the intramolecular interactions, rehybridization, and delocalization of ED within the compound as well as to inspect both the types of bonding, interactions between bonds, charge transfer and the conjugative interaction systems [25, 26]. **Table 3.9** gives detailed results of the NBO analysis showing as a significant hyper conjugative interaction: π (C18 - C19) → π* (C14 - C16) and π* (C7 - C12), π (C7 - C12) → π* (C18 - C19) and π* (C14 - C16), π (C21 - C32) → π* (C11 - C26), π (C14 - C16) → π* (C7 - C12) and π* (C18 - C19), π (C11 - C26) → π* (C28 - C30), π (C21 - C32) → π* (C28 - C30), π (C18 - C19) → π* (C14 - C16) and π* (C7 - C12), π (C28 - C30) → π* (C21 - C32) and π* (C11 - C26), π (C11 - C26) → π* (C21 - C32). Rest remaining transitions with higher E(2) values are lone pair LP(1) of N 4 → π* (O2 - C6), LP(2) of O2 → π* (N4 - C6), and π* (C5 - C6) and π* (C6), LP(2) of O3 → π* (C5 - C6), and π* (C5 - C8) and π* (C5), LP(3) OF Cl1 → π* (C18 - C19).

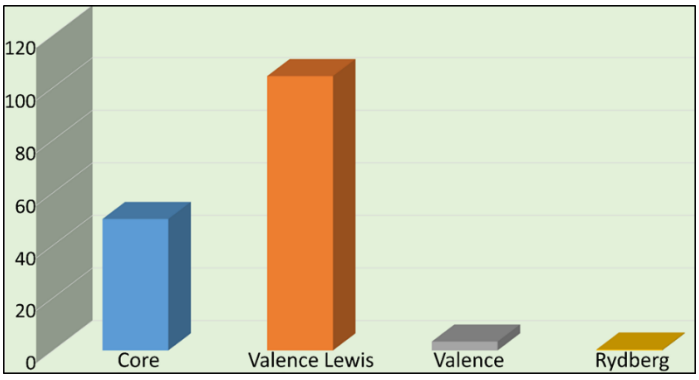

Figure 3.13. Percentage contribution of natural population analysis and natural Lewis structure of the compound 1.

Table 3.8. Summary of natural population analysis of the compound 1 obtained by B3LYP/6-311G (d, p).

Atom	Natural Charge	Natural population (*e*)			
		Core	Valence	Rydberg	Total
Cl1	-0.01417	9.99962	6.99538	0.01916	17.01417
O2	-0.62158	1.99977	6.61309	0.00872	8.62158
O3	-0.55055	1.99976	6.54092	0.00987	8.55055
N4	-0.59862	1.99928	5.58679	0.01254	7.59862
C5	0.54119	1.99932	3.41855	0.04094	5.45881
C6	0.5962	1.99928	3.35856	0.04596	5.4038
C7	-0.0181	1.99896	4.00225	0.01689	6.0181
C8	-0.47208	1.99912	4.4582	0.01477	6.47208
H9	0.2365	0	0.76052	0.00299	0.7635
H10	0.23698	0	0.76004	0.00298	0.76302
C11	-0.04086	1.99895	4.02608	0.01583	6.04086
C12	-0.18801	1.99899	4.17392	0.0151	6.18801
H13	0.20415	0	0.79301	0.00284	0.79585
C14	-0.18794	1.99899	4.17387	0.01509	6.18794
H15	0.2042	0	0.79296	0.00284	0.7958
C16	-0.2187	1.99892	4.20153	0.01825	6.2187
H17	0.21804	0	0.77889	0.00307	0.78196
C18	-0.02014	1.99852	3.99885	0.02276	6.02014
C19	-0.2188	1.99892	4.20163	0.01824	6.2188
H20	0.21799	0	0.77894	0.00307	0.78201
C21	-0.1946	1.999	4.17995	0.01565	6.1946
H22	0.20633	0	0.79075	0.00292	0.79367
C23	-0.19361	1.9991	4.17326	0.02124	6.19361
H24	0.22782	0	0.76797	0.00421	0.77218
H25	0.19147	0	0.80563	0.0029	0.80853
C26	-0.20319	1.999	4.18848	0.0157	6.20319
H27	0.19956	0	0.79741	0.00303	0.80044
C28	-0.19026	1.9991	4.17548	0.01567	6.19026
H29	0.20248	0	0.79503	0.00249	0.79752
C30	-0.19702	1.99911	4.18238	0.01554	6.19702
H31	0.20233	0	0.79522	0.00244	0.79767
C32	-0.18865	1.9991	4.17408	0.01547	6.18865
H33	0.20264	0	0.79488	0.00249	0.79736
C34	-0.3959	1.99915	4.37796	0.01879	6.3959
H35	0.20991	0	0.78652	0.00356	0.79009
H36	0.2099	0	0.78654	0.00356	0.7901
H37	0.40507	0	0.5895	0.00543	0.59493

Table 3.9. Second order perturbation theory of the Fock matrix NBO analysis.

Donor	Type	ED/e	Acceptor	Type	ED/e	E(2) kcal/mol	E(j)-E(i) a.u.	F(i,j) a.u.

C18 - C19	π	C14 - C16	π^*	248.99	0.01	0.081
C18 - C19	π	C7 - C12	π^*	177.81	0.02	0.084
N 4	LP1	O2 - C6	π^*	71.89	0.27	0.125
C7 - C12	π	C18 - C19	π^*	22.91	0.27	0.071
O2	LP2	N4 - C6	π^*	22.78	0.75	0.118
O2	LP2	C5 - C6	π^*	22.65	0.59	0.104
O3	LP2	C5 - C6	π^*	22.28	0.63	0.106
C21 - C32	π	C11 - C26	π^*	21.09	0.29	0.07
C14 - C16	π	C7 - C12	π^*	20.86	0.29	0.07
C14 - C16	π	C18 - C19	π^*	20.73	0.27	0.068
C7 - C12	π	C14 - C16	π^*	20.43	0.28	0.068
C11 - C26	π	C28 - C30	π^*	20.27	0.29	0.068
C21 - C32	π	C28 - C30	π^*	20.2	0.28	0.068
C18 - C19	π	C14 - C16	π^*	20.19	0.3	0.069
C28 - C30	π	C21 - C32	π^*	20.15	0.29	0.068
C28 - C30	π	C11 - C26	π^*	20.14	0.29	0.068
C11 - C26	π	C21 - C32	π^*	19.67	0.29	0.067
O3	LP2	C5 - C8	π^*	18.81	0.69	0.103
O2	LP2	C6	π^*	14.54	1.59	0.136
O3	LP2	C5	π^*	14.47	1.48	0.131
Cl1	LP3	C18 - C19	π^*	12.09	0.33	0.062

3.3.12. NMR Spectra

The experimental ^{1}H and ^{13}C NMR spectra of compound **1** were recorded using $CDCl_3$ solvent as shown in **Figure 3.14**. The GIAO (Gaussian with Gauge Independent Atomic Orbital) technique was applied to find out theoretical ^{1}H and ^{13}C chemical shifts in chloroform solvent, as illustrated in **Figure 3.15**, the peaks at 7.37, 7.32, 7.29, 7.26, and 7.26 *ppm* experimentally and theoretically at 7.47, 7.53, 7.57, 7.53, and 7.38 *ppm* are due to –CH (aromatic) protons. The NH proton has appeared at 7.24 *ppm* experimentally and theoretically at 6.93 *ppm*. The benzylic

CH_2 proton appeared at 4.49 ppm experimentally and theoretically at 4.52 *ppm*. The beta and gamma saturated -CH proton appeared at 2.94 and 3.31 *ppm* respectively experimentally and theoretically at 2.62 and 3.17 *ppm*.

Figure 3.14B showed the experimental ^{13}C NMR spectrum of the compound **1**, illustrating that the carbonyl peak at α-position was observed at 197.85 ppm and the amide carbonyl peak appeared at 159.71 *ppm*, similarily both the carbonyl peaks appear at 208.04 and 161.84 *ppm* in the theoretically calculated spectra (**Figure 3.15B**). The β and γ carbon atoms attached to the α-carbonyl carbon appeared experimental at 38.24 and 28.50 *ppm*, respectively (theoretically at 45.31 and 32. 07 ppm, respectively). The benzylic CH_2 carbon peak appeared at 43.47 *ppm* experimentally and at 45.94 *ppm* theoretically. The aromatic three quaternary carbon peaks appeared at 138.76, 136.84 & 132.07 *ppm* and 147.31, 145.49, & 145.27 *ppm* for experimental spectra and theoretically calculated spectra, respectively. The rest of the aromatic tertiary carbon peak was observed at 129.78 (2CH), 128.88 (2CH), 128.63 (2CH), 127.95 (2CH), 127.92 (CH) *ppm* experimentally and theoretically at 134.94, 134.03, 133.95, 133.82, 133.52, 133.27, 132.65 *ppm*, respectively.

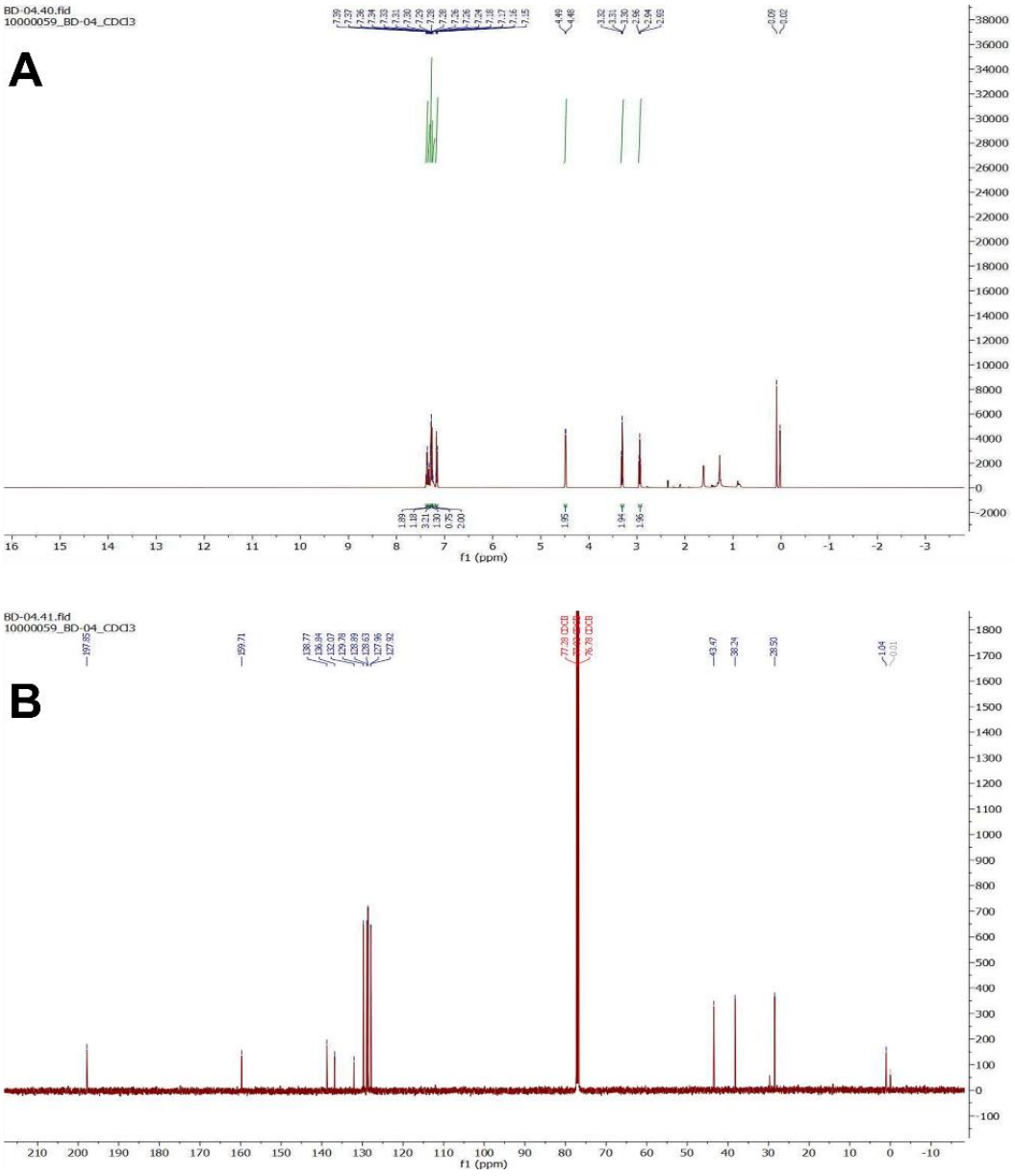

Figure 3.14. Experimental (A) ^{1}H and (B) ^{13}C spectra of compound 1.

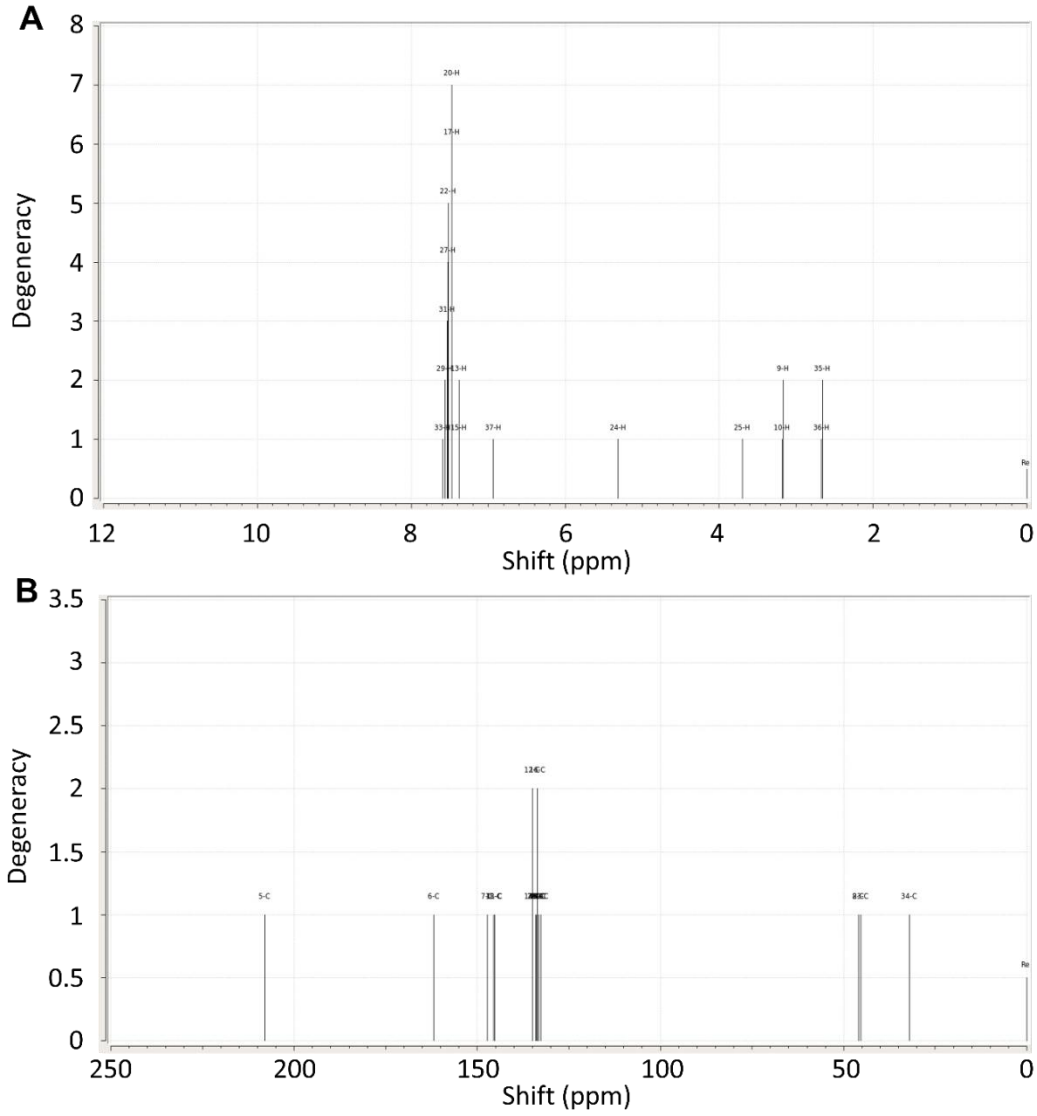

Figure 3.15. (A) Theoretical ^{1}H (B) ^{13}C spectra of compound 1.

3.3.13. In Vitro Biological Evaluation

3.3.13.1. Effect of compound 1 on Aβ$_{42}$ aggregation

We evaluated the effect of the compound 1 on the aggregation of Aβ$_{42}$ peptides using the ThT assay. The results shown in **Figure 3.16** indicated that compound 1 inhibited the aggregation of Aβ_{42} peptides at 1.6 μM while accelerated the aggregation at higher concentration ranging from 3.1- 50 μM. Moreover, there was a linear correlation between the effect on Aβ$_{42}$ aggregation and the concentration of the compound indicated by a correlation coefficient of

0.82 (**Figure 3.16B**). Aβ aggregation is one of the major player driving the pathogenesis of AD and considered as a drug target. The inhibitors of Aβ aggregation are continuously explored as potential therapeutics, however, recently promotors of Aβ aggregation have been proposed as potential therapeutics owing their role in converting the toxic oligomers into non-toxic fibrils at a faster rate.

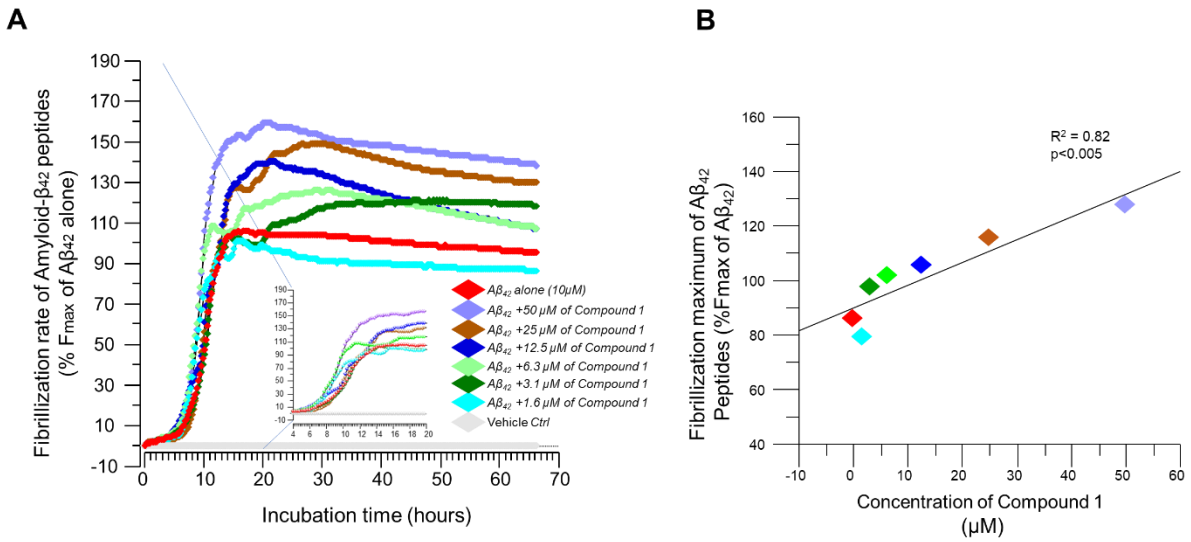

Figure 3.16. Effect of compound 1 on the Aβ42 peptide aggregation. A) shows the lag time, the rate, and the maximum fibrillization level of Aβ_{42} peptides in the absence and presence of various concentrations of compound **1**. The inset in **A** shows the first 20 hours of the process. The data are presented as a percentage of the average fibrillization maximum (F_{max}) of 10 μM Aβ_{42} alone (red line). The average Fmax was calculated based on all readings of the Aβ_{42} graph between 20 to 68 hours. **B**) illustrates a strong positive correlation between the F_{max} of Aβ_{42} and the concentration of compound **1**.

3.3.13.2. In Vitro Cellular Toxicity Assay

In order to evaluate the cellular toxicity of compound **1**, *in vitro* MTT assay was performed at a final concentration of 1, 10 & 50 μM against NCI-H69, NCI-H82, and A549 cell lines. Compound **1** did not show any toxicity after a treatment period of 24 and 48 hrs (**Figure 3.17**) indicating its safety in biological applications.

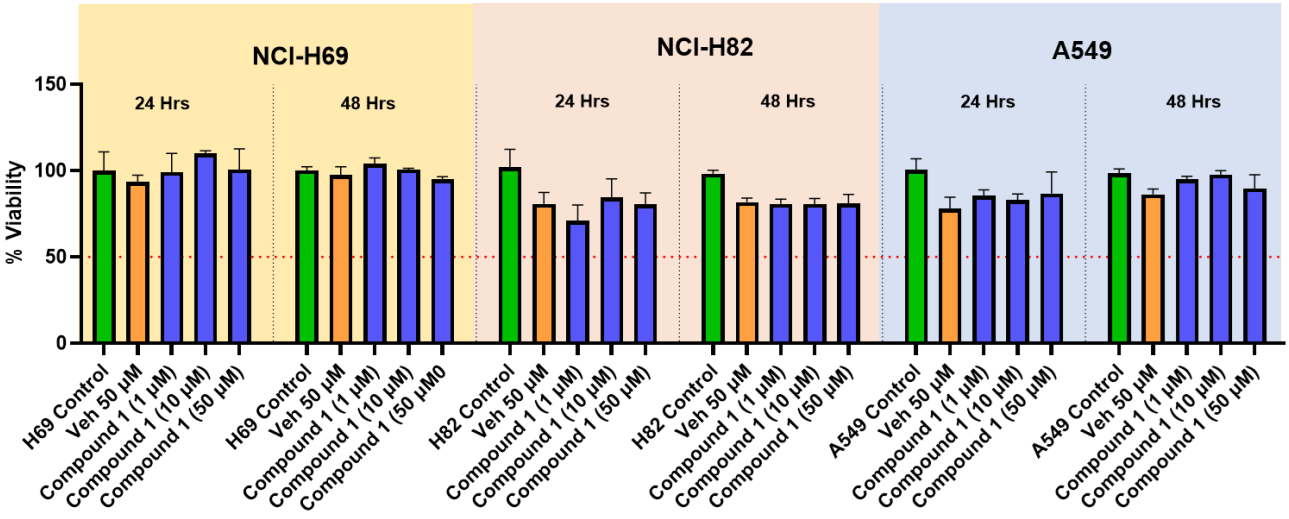

Figure 3.17. MTT-based in vitro cell viability assay of the compound 1 using NCI-H69, NCI-H82, and A549 cell lines. Data are expressed as % mean values ±SD of quadruplicate data points. The viability of the control well is considered as 100 %.

3.3.14. Molecular Docking Study

In order to determine the binding interactions of compound 1 with Aβ monomer and Aβ pentamer, we performed molecular docking by using AutoDock tool (ADT) [27]. This finding suggested that the compound 1 modulates the $A\beta_{42}$ aggregation by showing various intermolecular interactions with the $A\beta_{42}$ monomer and fibrils residues**.** The $A\beta_{42}$ fibril (PDB: 2BEG) containing 5 β-sheet units and $A\beta_{42}$ monomer (1IYT) were downloaded from the protein data bank [28]. For the processing of $A\beta_{42}$ pentamer and monomer, water molecules are deleted and all necessary hydrogen bonds and Kohlmann charges are added by using ADT [29, 30]. The best docking pose of compound 1 gave a binding affinity of -8.2 kcal/mol with Aβ fibrils and -4.999 kcal/mol with Aβ monomer**.** The 3D and 2D interaction of the compound 1 with Aβ pentamer (**Figure 3.18B & Figure 3.18C**) revealed that the it was encased in the hydrophobic pocket formed by the residues LEU17, PHE19, VAL40. The π-electrons of the phenyl ring and 4-chlorobenzene ring undergo π-π T shaped interaction and π-alkyl interaction with the residues PHE19 and LEU17, VAL40 respectively of various chains of Aβ pentamer.

The loan pairs on chlorine atom also showed π-alkyl interaction with PHE19 residue. The amine hydrogen atom formed conventional hydrogen bonding with LEU17 residue. Likewise, the 3D and 2D interacts of compound 1 with Aβ monomer (1IYT) revealed that the benzyl group showed polar interaction with the residue GLN15 and the 4-chloro phenyl group undergoes hydrophobic interaction with PHE19 residue. The molecule also showed positive ion interaction with LYS16 residue.

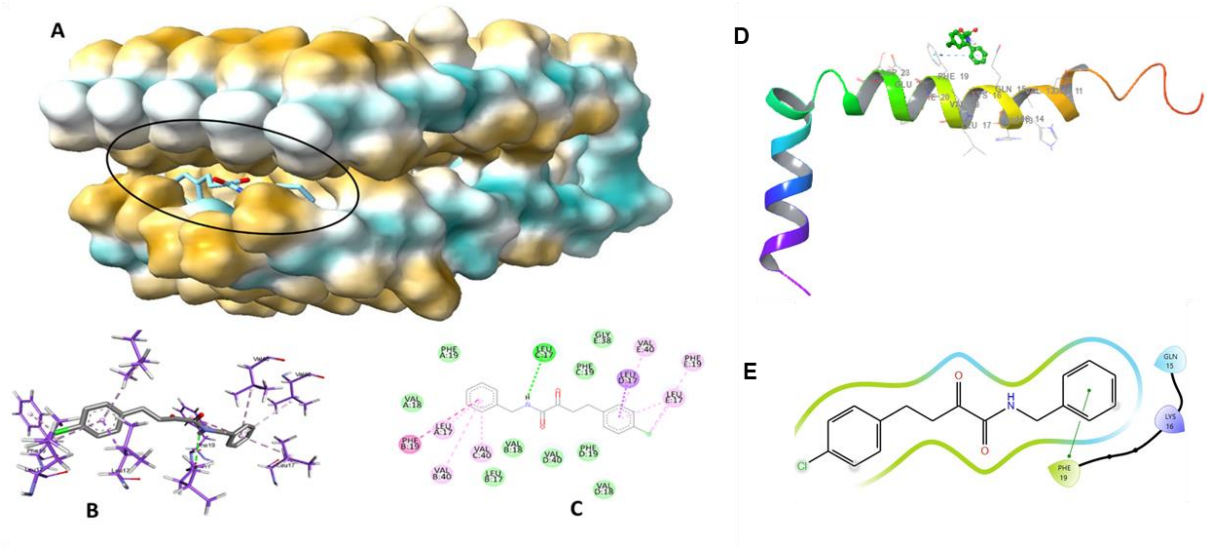

Figure 3.18. Molecular Docking of compound 1 against Aβ. (A) Docking of compound 1 into the $A\beta_{42}$ pentamer (PDB: 2BEG). (**B**) Three-dimensional (3D) and (**C**) Two-dimensional (2D) binding interactions of compound **1** with $A\beta_{42}$ binding pocket. (D) 3D (E) 2D binding interaction of compound 1 with $A\beta_{42}$ monomer (PDB:1IYT).

3.3.15. Molecular Dynamics Simulation

In order to better understand the dynamic behavior of protein and ligand we have performed MD simulation of complex of compound 1 with Aβ monomer and fibril for 200 ns. The results from the MD trajectory analysis are shown in **Figure 3.19**. The RMSD (Root Mean Square Deviation) is frequently employed to assess the stability and conformational changes of both the protein and the ligand during the simulation.

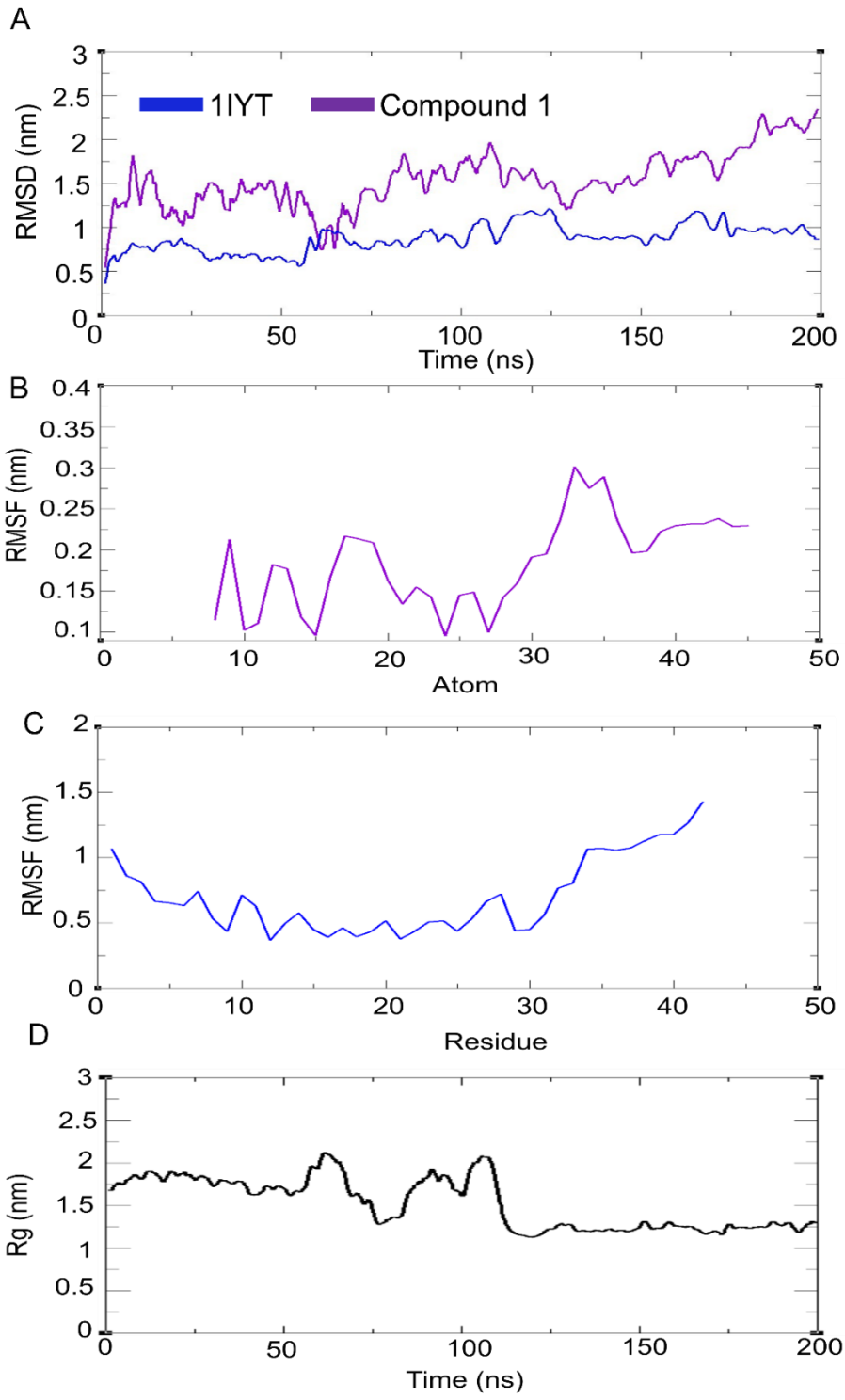

Figure 3.19. Molecular dynamics trajectory analysis of compound 1-Aβ monomer complex. (A) RMSD (Root Mean Square Deviation) (B) RMSF (Root Mean Square Fluctuation) of ligand (C) RMSF of protein, (D) Radiation of Gyration of the complex.

The Root Mean Square Deviation (RMSD) of ligand and monomer Aβ (1IYT) in **Figure 3.19A** fluctuated in between the value 0.5 to 2nm which indicates the stability of the complex. Root means square fluctuation (RMSF) provides insights into the flexibility and dynamic behavior of individual residues or atoms during the simulation period. RMSF value of ligand was found at 0.1 to 0.25 nm suggesting the flexibility and stability of the ligand (**Figure 3.19B)** and similarly, RMSF value for protein was found was found between 0.5 to 1.5 nm indicating the flexibility of the Aβ monomer to interact with the compound 1 (**Figure 3.19C**). The radiation of gyration value indicated that the fluctuation is between 50 to 120 ns but remains stable for the rest of the simulation period (**Figure 3.19D**). The average number of H-bond formed during the 200 ns simulation with the cut-off value set at 0.35 nm was estimated for the complex compound 1 with the monomer Aβ protein (**Figure 3.20A**). There seems to be missing instances of H-bond formation between compound 1 and monomer Aβ in between the 30 to 170 ns time interval of the simulation, followed by an average of 1-2 H- bond formation during the 200 ns simulation (**Figure 3.20A**). From the hydrogen bond distance (HBD) shown in (**Figure 3.20B**) it can be seen that the average H-bond distance was maintained about 0.3 nm.

Similarly, by using the same methods we have also performed MD simulation of compound 1 with the pentamer of Aβ evaluating the stability of the complex for 200 ns. The RMSD of the ligand and protein showed fluctuation between 0.5 to 2.5 nm and 0.5 to 1 nm respectively indicating the stability of the complex. At the first period of 30 ns, the ligand showed more fluctuation but remained stable for the rest of the simulation period. The RMSF value of ligands was found between 0.1 to 0.3 nm indicating the flexibility and stability of the complex. The Rg value showed that there is no fluctuation for the complex and remains stable for the whole of the simulation period indicating that the complex is more stable.

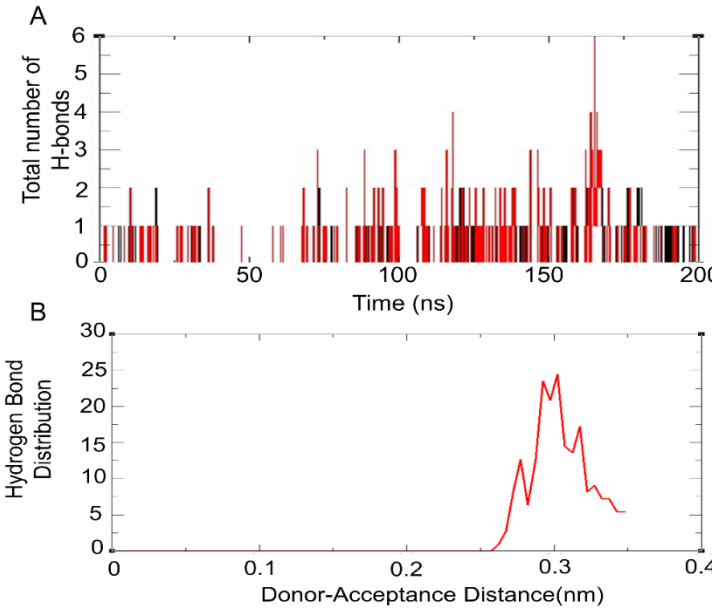

Figure 3.20. Hydrogen bond analysis of the compound 1-Aβ-monomer complex MD trajectory. (A) Total number of H-bonds, and (B) Hydrogen bond distribution.

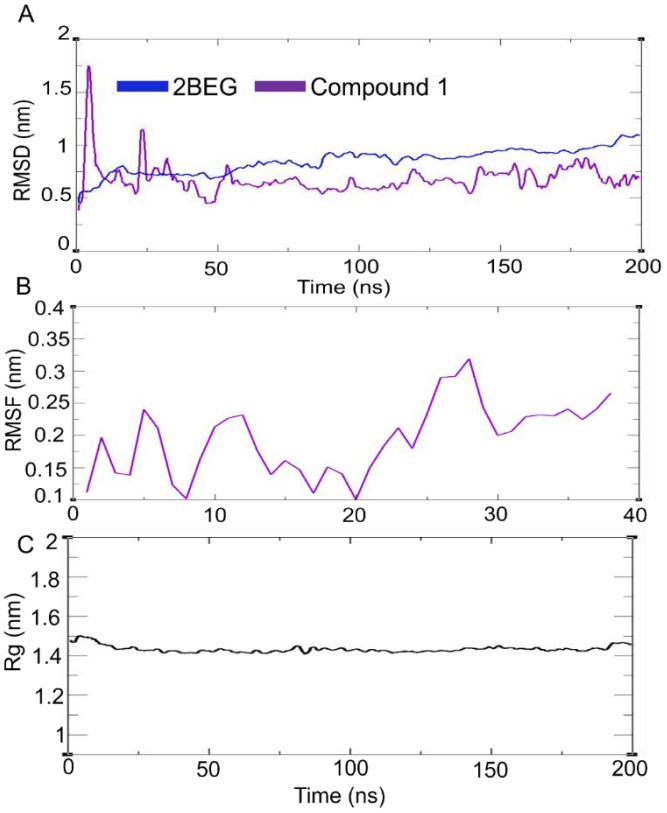

Figure 3.21. Molecular dynamics trajectory analysis of compound 1-Aβ pentamer complex. (A RMSD (B) RMSF of ligand (C) Radiation of Gyration of the complex.

The average number of H-bond formation during the 200 ns simulation with the cut-off value set at 0.35 nm was estimated for the complex compound 1 with the pentamer Aβ (**Figure 3.22A**). There seems to be missing instances of H-bond formation between compound 1 and pentamer Aβ in between the 140 to 160 ns time interval of the simulation, followed by an average of 1-2 H- bond formation during the 200 ns simulation. Hydrogen bond distance (HBD) shown in (**Figure 3.22B**) it can be seen that the average H-bond distance was maintained at about 0.3 nm.

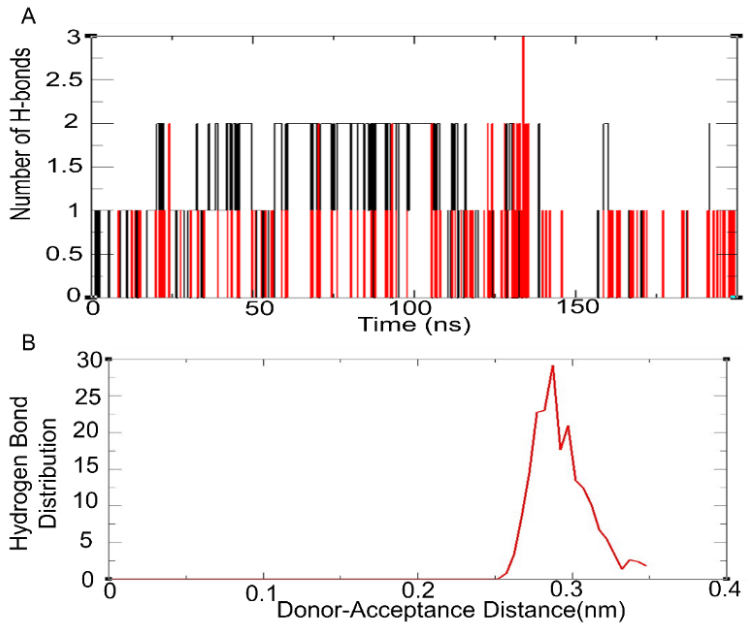

Figure 3.22. Hydrogen bond analysis of the compound 1-Aβ pentamer complex MD trajectory. (A) Total number of H-bonds, and (B) Hydrogen bond distribution.

3.3.15.1. Principal Component Analysis

Principal Component Analysis (PCA), also known as essential dynamics, is a statistical technique frequently used in MD simulations to reduce the dimensionality of the data and capture the most significant modes of motion in biomolecules, such as proteins, nucleic acids, and their complexes. In MD simulations the motions of biomolecules can span a wide range of frequencies and amplitudes, from localized vibrations of individual atoms to large-scale domain movements. While the complete trajectories provide detailed insights, it's often beneficial to

focus on the primary modes of motion that contribute most to the overall dynamics. Covariance Matrix Construction it is the first step in PCA is to compute the covariance matrix of atomic positional fluctuations from the MD trajectory. This matrix captures the correlated motions between every pair of atoms. The first step in PCA analysis is the principal components of PCA analysis is eigenvectors which represents the directions of maximal variance (i.e., the main modes of motion) in the data. The eigenvalues give the magnitude of the variance along each of these directions**. Figure 3.23A** and **Figure 3.23C** represent the eigenvalues for the compound 1-Aβ monomer complex and compound 1-pentamer Aβ respectively.

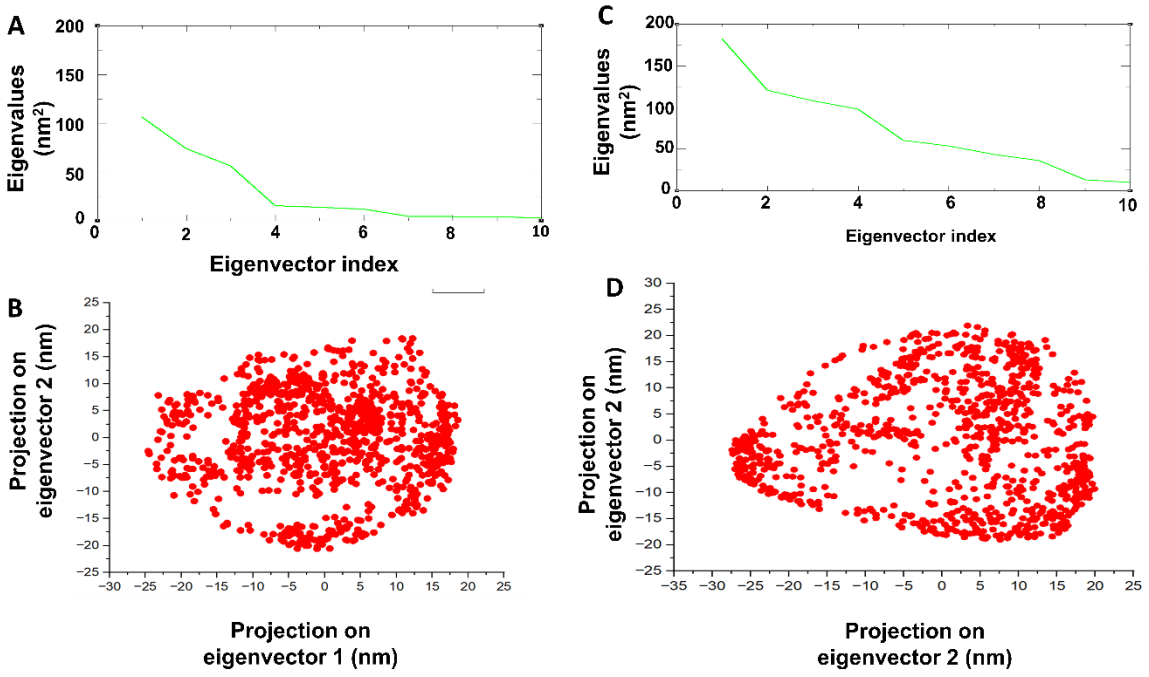

Figure 3.23. Eigenvalues and the 2D projection of the first two principal components of compound 1-Aβ monomer and compound 1-Aβ pentamer complex. **(**A) Eigenvalues of the first principal components of the simulated system for the compound 1-Aβ monomer complex, (B) The 2D projection of the first two principal components for the compound 1-Aβ monomer complex. **(**C) Eigenvalues of the first principal components of the simulated system for the compound 1-Aβ pentamer complex, (B) The 2D projection of the first two principal components for the compound 1-Aβ pentamer complex.

The plot in **Figure 3.23A** shows that the eigenvalues after the fourth principal component starts to make a straight horizontal line in the case of the compound 1-Aβ monomer complex that analysis suggests that the first four PC eigenvector accounts for most of the motions in the system. Similarly, in **Figure 3.23C,** the plot shows that the eigenvalues after the ninth principal component start to make a straight horizontal line in the case of the complex compound 1-Aβ pentamer that analysis suggests that the first ninth PC eigenvector accounts for most of the motions in the system.

In the delineated 2D representation, based on the first two principal components (as shown in **Figure 3.23B** and **Figure 3.23D**), the diverse conformations adopted by the protein throughout the simulation period are evident. The dense clustering observed in **Figure 3.23B**, in contrast to the expansive distribution in **Figure 3.23D**, suggests a heightened stability of the complex across the conformational landscape.

3.3.15.2. Free Energy Landscape Analysis

Free energy landscape (FEL) analysis in molecular dynamics (MD) simulations is a powerful technique used to understand the thermodynamic and kinetic properties of complex molecular systems. It allows researchers to explore the energy landscape of a system, identify stable and metastable states, and calculate thermodynamic quantities such as free energy differences, potential of mean force (PMF) profiles, and transition pathways. In order to check the possible confirmations taken by the Aβ as well as to calculate the Gibbs free energy during the simulation period we have performed FEL analysis. FEL can be representative of two variables that can directly reflect the distinctive properties of the system and measure the conformational changes. The FEL serves as an indicator for two crucial factors that highlight the unique characteristics of the system and track alterations in its conformation. To map out the free energy minimum landscape for compound 1 with Aβ monomer and with pentamer, we evaluated the FEL in the context of RoG and RMSD as the primary reaction coordinates, as

depicted in **Figures 3.24**. This FEL analysis uncovers fluctuations in the Gibbs free energy (ΔG), with values oscillating between 0 and 10.30 kJ/mol for the examined complexes. An in-depth look at the energy landscape allowed us to discern its shape and dimensions. Here, small, centralized blue regions suggest a complex within the cluster exhibiting maximum stability and minimum energy. The slender funnel visible in the 3D visualizations signifies the dynamic conformational shifts over time, driving the system towards adopting a native structure at its energy optimum.

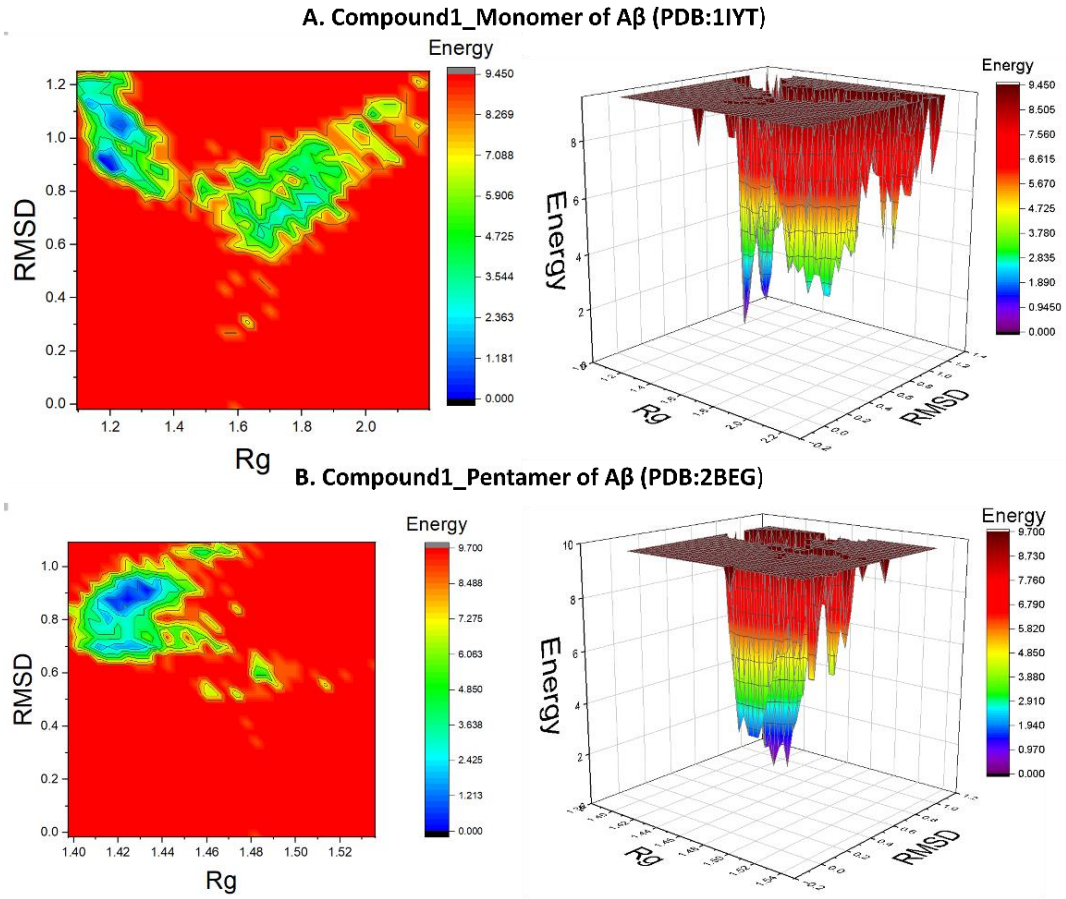

Figure 3.24. The 2D and 3D free energy landscape diagram as a function of RMSD and RoG as the two coordinates of the compound 1-Aβ monomer complex and 1-Aβ pentamer complex. The free energy is displayed in terms of kj/mol where the purple Colour indicates the least energy and red the highest energy. The folding funnel formed by the compound 1-Aβ pentamer complex shows stable folding. The compound 1-Aβ pentamer complex showed less number of funnel than the monomer of Aβ suggesting stability of the complex.

The FEL analysis revealed that the ΔG values of compound 1 formed complexed with Aβ pentamer (2BEG) protein (**Figure 3.24B**), converged to an energy minimum state which is illustrated in the overall 3D plots as a smaller number of funnel formed for the compound 1-Aβ pentamer complex. This along with the 2D contour plot clearly illustrates that in the simulated system compound 1-Aβ pentamer complex reached a single distinct local energy minima and hence a stable folding state. However, an exception was observed for the compound 1-Aβ monomer complex (**Figure 3.24A**) where the 3D plot shows multiple distinct funnel formations, indicating that the folding process is not too gradual in reaching the global energy minima.

3.4. Materials and Methods

3.4.1. Materials

All the chemicals and solvents used for the synthesis of the compound 1 were purchased from Sigma-Aldrich and used as obtained without further purification.

3.4.2. Instrumentation Details

^{1}H and ^{13}C NMR spectroscopy were recorded in $CDCl_3$ at 25 °C on an AVH -500 AVANCE III HD, 500 MHz spectrometers at the Central Instrumentation Facility, IIT (BHU), Varanasi. The Chemical shift values are expressed as δ value (ppm) downfield with residual protons of the solvent (CDCl3, δ = 7.26 ppm) as the internal standard. Fourier transform infrared (FT-IR) spectra were recorded on ATR, Department of Pharmaceutical Engineering & Technology, IIT (BHU). UV-Visible spectra have been recorded by using Agilent. UV-Visible spectrometer, IIT (BHU).

3.4.3. Synthesis of *N*-benzyl-4-(4-chlorophenyl)-2-oxobutanamide (1)

β, γ-Unsaturated α-hydroxy thioesters : 4 (0.05 g, 1.0 equiv) was dissolved in dry toluene (1.0 mL), and the benzylamine (5.0 equiv) was added to the reaction mixture. The reaction mixture

was allowed to stir at room temperature for 20- 30 min. After completion of the reaction, water was added, and the product was extracted with DCM. The combined organic layers were dried over anhydrous Na_2SO_4 and filtered, and the filtrate was concentrated under reduced pressure to get a residue. The crude residue was purified over silica gel column chromatography [100−200], eluent: ethyl acetate/n-hexane] to obtain the pure product. **^{1}H NMR (500 MHz, $CDCl_3$): δ** 7.39 – 7.35 (m, 2H), 7.35 – 7.31 (m, 1H), 7.29 (dd, J = 6.6, 2.6 Hz, 3H), 7.26 (s, 1H), 7.24 (s, 1H), 7.16 (d, J = 8.4 Hz, 2H), 4.49 (d, J = 6.1 Hz, 2H), 3.31 (d, J = 7.5 Hz, 2H), 2.94 (t, J = 7.4 Hz, 2H). **^{13}C NMR (126 MHz, $CDCl_3$) δ** 197.85 (s), 159.71 (s), 138.76 (s), 136.84 (s), 132.07 (s), 129.78 (s), 128.88 (s), 128.63 (s), 127.94 (s), 43.47 (s), 38.24 (s), 29.71 (s), 28.50 (s). IR ν (cm^{-1}) – 660.34, 694.69, 734.28, 749.78, 809.61, 843.56, 906.15, 956.78, 1011.87, 1083.65, 1108.41, 1222.56, 1245.84, 1288.58, 1365.66, 1391.97, 1452.42, 1488.92, 1524.89, 1656.26, 1716.57, 1744.31, 2852.72, 2921.81, 3028.01, 3298.15.

3.4.4. Single crystal X-Ray diffraction

Suitable crystals were grown by slow evaporation of the methanol and dichloromethane (DCM) (1:1) solution of the compound 1. A suitable single crystal was carefully picked under a polarizing microscope and glued on to a very thin glass fiber with the help of cyanoacrylate (superglue) adhesive. The single-crystal X-ray data collection was carried out at Bruker D8 Quest PHOTON II diffractometer with monochromatic Mo Kα radiation (λ = 0.71073 *Å*) at 296(2) *K* operating at 50 *kV* voltage and 20 mA current by using ω and ϕ scan. The diffraction profiles were integrated with the SAINT program [31] and the obtained data sets were reduced using the APEX3 software. Numerical absorption corrections (multi scan) were performed with SADABS program [32]. The structure was solved by the full matrix least-square method on F^2 using SHELXL-2016 [33] present in the WINGX package of programs (Version 2018-3) [14]. All the non-hydrogen atomic sites in the present structure were located successfully in different Fourier maps and finally refined with anisotropic displacement parameters. Hydrogen atoms

were fixed geometrically in calculated positions and refined using the riding model. One can find the B-level alert in the Check CIF report for the compound 1 which is mainly due to the significant disorderness of carbon atoms for which no further modelling was attempted. Such disorderness of sp^3 hybridized carbon atoms can often show the bond length variation in flexible chain structure. The details about the crystal structure solution and final refinement parameter for the compound 1 is listed in **Table 3.1**. Selected bond distances and angles are given in **Table 3.6**. The crystallographic files can be obtained for the compound 1 from the Cambridge Crystallographic Data Center (CCDC No. 2196203) via www.ccdc.cam.ac.uk/data_request/cif.

3.4.5. Computational Details

DFT is a key *in silico* tool for investigating the electronic structure (primarily the ground state) of quantum mechanical systems. The three-dimensional molecular geometrical structure of the single crystal was optimized by DFT calculations with the help of Becke's three-parameter hybrid exchange functional and the Lee, Yang, and Parr B3LYP/6-311G (d, p) basis sets [34] using the Gaussian 16 software package [35, 36]. B3LYP is the most widely used DFT approach because it is capable of accurately predicting molecular structures and other properties [37]. Previous literature revealed that greater basis sets should produce superior and more reliable results as 311G(d,p) basis set uses divergent exponents for the polarization functions on different nuclei. This basis set provides more accuracy and authentic result as compared to other basis sets [38, 39]. The vibrational data was generated using the optimized geometry with the help of the same basis set and computational method. The ^{1}H and ^{13}C NMR chemical shifts were calculated using the optimized parameters obtained from the B3LYP/ 6-311G (d,p) method in deuterated chloroform ($CDCl_3$) as solvent where the solvent effect was also taken into account using CPCM model using the Gauge-Including Atomic Orbitals DFT method (GIAO–DFT), where tetramethylsilane (TMS) was taken as a reference [40]. Crystal Explorer version 21.5 software was used to construct the molecule's HS and fingerprint plots (FPs)[12].

The energy framework and all the possible interactions were calculated by using B3LYP/6–311 G (d, p) energy model present in the Crystal Explorer software version 21.5 [8, 41]. Further, molecular docking was performed by using the Autodock Vina tool (ADT) 1.5.6, and all the 2D and 3D interactions are generated by using Biovia Discovery studio 2021 [42, 43].

3.4.6. Molecular Dynamics Simulation

The MD simulation of a complex of compound 1-Aβ monomer and compound 1-Aβ pentamer for 200 ns was performed by using the software GROMACS 2020.3. The initial setup for this simulation, specifically the movement characterization of the protein, was achieved through the CHARM-GUI webserver, which employs the Charm 36 forcefield. In order to ensure the reliability and consistency of the simulation, we adhered to conditions like the constant number, volume, and temperature (NVT) ensemble, as well as the isothermal-isobaric (NPT) ensemble. A comprehensive breakdown of the parameters and the rationale behind our simulation approach can be found in earlier literature [44, 45].

3.4.7. Biological Evaluation Details

3.4.7.1. Aβ aggregation assay

The effect of compound **1** was evaluated on the aggregation of amyloid beta 1-42 (Aβ_{42}) using earlier reported method [46]. Briefly, ultrapure, hexafluoroisopropanol (HFIP)-treated, recombinant Aβ_{42} peptides (Aβ_{42}, catalogue number A-1002, rPeptide) were used. A 500 μM Aβ_{42} peptide stock solutions were prepared in DMSO (dimethyl sulphoxide, D2650, Sigma) by rigorous vortexing, and finally filtering the solution through a 0.2 -*mm* filter unit (Spartan 3/0.2 PA, Whatman Group). The stock solutions were freshly prepared, based on the molecular weight of the peptides provided by the manufacturer. Compound **1** was also dissolved in DMSO at a stock concentration of 100 *mM*. The assay buffer was PBS (pH = 7.4). All samples were applied in sextuplicate in the wells of a microtiter plate [(NUN96fb_LumiNunc FluoroNunc)

Nunclon 96 Flat Black, DK]. First, 50 μL of a serial working solution of compound **1** was applied to the assigned wells. The compound **1** solutions were prepared in PBS as a two-fold serial dilution to achieve the final concentrations of 50 μM to 1.6 μM in the reaction mixture in the well. Then 50 μM of a freshly prepared working solution of Aβ_{42} (30 μM) in PBS was added to all wells with the exception of the control wells (in which just vehicle solution was added). Finally, 50 μL of a freshly prepared working solution of thioflavin-T (ThT, 3.75 μM) in PBS was added to all wells including the blanks and controls. The final volume of the reaction mixture was 150 μL, bringing the final concentration of A$\beta_{1\text{-}42}$ to 10 μM and the ThT to 1.25 μM. The plate was then carefully sealed with tape (Nunc, #236366, DK) and then further sealed with the lock on using parafilm to avoid evaporation. All the wells at the four sides of the plates contained only blank solutions to further prevent evaporation in the reaction wells. Continuous incubation and reading took place in a SpectraMax i3x spectrophotometer at 37 $^{\circ}$C. The kinetic bottom-reading function was set at 15-min intervals with 5s orbital shaking prior to each reading at 445 nm excitation wavelength and 490 nm as the emission wavelength.

3.4.7.2. In Vitro Cellular Toxicity Assay

In vitro cellular toxicity of the compound **1** was evaluated at 1, 10 & 50 μM concentrations against NCI-H69, NCI-H82, and A549 cell lines using an MTT assay [47]. Briefly, NCI-H69, NCI-H82, and A549 cell lines were cultured using RPMI-1640 supplemented with 10% FBS, penicillin, and streptomycin at 37 ºC and 5% CO_2 in a humidified incubator in 96 well plates at a confluency of 70-80 %. Further, the cell lines were treated with compound 1 at a final concentration of 1, 10 & 50 µM using a 100 mM stock in DMSO. At the end of the treatment period (24 & 48 hrs), 10 μl of 12 mM (5 mg/ml) 3-(4,5-dimethylthiazol-2-yl)-2,5-diphenyltetrazolium bromide (MTT) (Sigma) dissolved in phosphate buffer saline pH 7.4 was added to each well of the plate and incubated for 4 hours at 37 °C in the CO_2 incubator. After the incubation, the reaction was stopped by adding 100 µl of the stop solution (10 % SDS in

0.01M HCl) and incubated overnight to dissolve the formazan crystals. Finally, the absorbance was measured at 570 nm on Tecan spectrophotometer.

The percentage cell viability was calculated using the following formula using DMSO control as 100%:

$$\text{Percentage cell viability} = \frac{OD\ of\ sample}{OD\ of\ control} * 100$$

3.5. Conclusion

In this chapter, we have explored the synthesis of α-ketoamide compound 1 from β,γ-unsaturated α-ketothioester and reported its single crystal XRD structure. Experimental bond angle and bond length, overall packing structure, and intermolecular well as intramolecular interaction were well determined from the crystal structure of compound 1. Hirschfeld analysis and energy framework calculation were performed in order to determine different surface interactions. Theoretical quantum calculations such as Density-Functional Theory (DFT) help to understand the electronic structure, stability, and reactivity of a compound. So, in order to better comprehend the stability and reactivity of the α-ketoamide, we performed the theoretical calculation for compound 1. Additionally, DFT calculation has been performed to determine the optimized stable structure in the gas phase, HOMO-LUMO calculation determined the stability of the compound 1, and the reactive sites of compound 1 were determined from Mulliken atomic charge, molecular electrostatic potential (MEP), and NBO analysis. Further, the in vitro biological evaluation of compound 1 revealed that it is a potential modulator of Aβ aggregation by inhibiting Aβ aggregation at low micromolar concentration and accelerating the conversion of small, toxic Aβ oligomers to matured nontoxic pentamer at high concentrations. Moreover, compound 1 did not show cytotoxicity in the MTT assay against three different cell lines. the molecular docking investigation demonstrated the binding interactions of compound 1 with both Aβ monomer and Aβ pentamer. The stability of this complex was subsequently ascertained through molecular dynamics analysis. These findings underscore the potential for

further exploration of α-ketoamide derivatives as therapeutic agents against Alzheimer's Disease (AD).

3.6. References

1. D. Cuerrier, T. Moldoveanu, J. Inoue, P. Davies, R. Campbell, Calpain inhibition by α-ketoamide and cyclic hemiacetal inhibitors revealed by X-ray crystallography, Biochemistry, 45 (2006) 7446-7452.
2. M. Wang, Z. Dai, X. Jiang, Design and application of α-ketothioesters as 1,2-dicarbonyl-forming reagents, Nature communications, 10 (2019) 2661.
3. S.L. Harbeson, S.M. Abelleira, A. Akiyama, R. Barrett III, R.M. Carroll, J.A. Straub, J.N. Tkacz, C. Wu, G.F. Musso, Stereospecific synthesis of peptidyl. alpha.-keto amides as inhibitors of calpain, Journal of medicinal chemistry, 37 (1994) 2918-2929.
4. J.J. Chen, S.V. Deshpande, Rapid synthesis of α-ketoamides using microwave irradiation–simultaneous cooling method, Tetrahedron Letters, 44 (2003) 8873-8876.
5. C. De Risi, G.P. Pollini, V. Zanirato, Recent developments in general methodologies for the synthesis of α-ketoamides, Chemical Reviews, 116 (2016) 3241-3305.
6. D. Kumar, S.R. Vemula, G.R. Cook, Recent advances in the catalytic synthesis of α-ketoamides, ACS Catalysis, 6 (2016) 4920-4945.
7. R. Maity, B. Das, I. Das, Transition-Metal-Free Reduction of α-Keto Thioesters with Hydrosilanes at Room Temperature: Divergent Synthesis through Reagent-Controlled Chemoselectivities, Advanced Synthesis & Catalysis, 361 (2019) 2347-2353.
8. P.R. Spackman, M.J. Turner, J.J. McKinnon, S.K. Wolff, D.J. Grimwood, D. Jayatilaka, M.A. Spackman, CrystalExplorer: A program for Hirshfeld surface analysis, visualization and quantitative analysis of molecular crystals, Journal of Applied Crystallography, 54 (2021) 1006-1011.
9. J.J. McKinnon, F.P. Fabbiani, M.A. Spackman, Comparison of polymorphic molecular crystal structures through Hirshfeld surface analysis, Crystal growth & design, 7 (2007) 755-769.
10. S.K. Seth, Structural elucidation and contribution of intermolecular interactions in O-hydroxy acyl aromatics: Insights from X-ray and Hirshfeld surface analysis, Journal of Molecular Structure, 1064 (2014) 70-75.
11. I. Feddaoui, M.S. Abdelbaky, S. García-Granda, K. Essalah, C.B. Nasr, M. Mrad, Synthesis, crystal structure, vibrational spectroscopy, DFT, optical study and thermal

analysis of a new stannate (IV) complex based on 2-ethyl-6-methylanilinium (C9H14N) 2 [SnCl6], Journal of Molecular Structure, 1186 (2019) 31-38.

12. S.P.T.M.M. JJ, Wolff SK Grimwood DJ Jayatilaka D, Spackman MA J. Appl. Crystallogr, 54 (2021) 1006-1011.
13. M.N. Slipchenko, B.G. Sartakov, A.F. Vilesov, S.S. Xantheas, Study of NH stretching vibrations in small ammonia clusters by infrared spectroscopy in He droplets and ab initio calculations, The Journal of Physical Chemistry A, 111 (2007) 7460-7471.
14. D. Wiles, T. Suprunchuk, The infrared absorption spectra of thiosemicarbazide and related compounds: NH2 and NH vibrations, Canadian Journal of Chemistry, 47 (1969) 1087-1089.
15. M. Margoshes, V. Fassel, The infrared spectra of aromatic compounds: I. The out-of-plane CH bending vibrations in the region 625–900 cm− 1, Spectrochimica Acta, 7 (1955) 14-24.
16. G. Suchkova, L. Maklakov, Amide bands in the IR spectra of urethanes, Vibrational Spectroscopy, 51 (2009) 333-339.
17. P. Kalsi, Spectroscopy of organic compounds, New age international, 2007.
18. E.S. Marinho, M.M. Marinho, A DFT study of synthetic drug topiroxostat: MEP, HOMO, LUMO, International Journal of Scientific & Engineering Research, 7 (2016).
19. V. Choudhary, A. Bhatt, D. Dash, N. Sharma, DFT calculations on molecular structures, HOMO–LUMO study, reactivity descriptors and spectral analyses of newly synthesized diorganotin (IV) 2-chloridophenylacetohydroxamate complexes, Journal of computational chemistry, 40 (2019) 2354-2363.
20. E.A. Eno, J.I. Mbonu, H. Louis, F.S. Patrick-Inezi, T.E. Gber, T.O. Unimuke, E.E. Okon, I. Benjamin, O.E. Offiong, Antimicrobial activities of 1-phenyl-3-methyl-4-trichloroacetyl-pyrazolone: Experimental, DFT studies, and molecular docking investigation, Journal of the Indian Chemical Society, 99 (2022) 100524.
21. P.W. Ayers, R.G. Parr, Variational principles for describing chemical reactions: the Fukui function and chemical hardness revisited, Journal of the American Chemical Society, 122 (2000) 2010-2018.
22. Z. Demircioğlu, Ç.A. Kaştaş, O. Büyükgüngör, The spectroscopic (FT-IR, UV–vis), Fukui function, NLO, NBO, NPA and tautomerism effect analysis of (E)-2-[(2-hydroxy-6-methoxybenzylidene) amino] benzonitrile, Spectrochimica Acta Part A: Molecular and Biomolecular Spectroscopy, 139 (2015) 539-548.

23. C. Morell, A. Grand, A. Toro-Labbé, New dual descriptor for chemical reactivity, The Journal of Physical Chemistry A, 109 (2005) 205-212.
24. R.P. Gangadharan, S.S. Krishnan, Natural Bond Orbital (NBO) Population Analysis of 1-Azanapthalene-8-ol, Acta Physica Polonica, A., 125 (2014).
25. A. Fatima, A. Ali, S. Shabbir, M. Khan, M. Mehkoom, S. Afzal, M. Ahmad, K. Althubeiti, N. Siddiqui, M. Singh, Synthesis, crystal structure, characterization, Hirshfeld analysis, molecular docking and DFT calculations of 5-Phenylamino-isophthalic acid: A good NLO material, Journal of Molecular Structure, 1261 (2022) 132791.
26. N.L. John, S. Abraham, J. George, P. Karuppasamy, M. Senthilpandian, P. Ramasamy, G. Vinitha, Synthesis, structure, NBO, Hirshfeld surface, NMR, HOMO-LUMO, UV, photoluminescence, z scan, vibrational and thermal analysis of piperazinedi-ium tetrakis (μ2-chloro)-diaqua-dichloro-di-cadmium single crystal, Journal of Molecular Structure, 1258 (2022) 132685.
27. N.T. Nguyen, T.H. Nguyen, T.N.H. Pham, N.T. Huy, M.V. Bay, M.Q. Pham, P.C. Nam, V.V. Vu, S.T. Ngo, Autodock vina adopts more accurate binding poses but autodock4 forms better binding affinity, Journal of Chemical Information and Modeling, 60 (2019) 204-211.
28. P.W. Rose, B. Beran, C. Bi, W.F. Bluhm, D. Dimitropoulos, D.S. Goodsell, A. Prlić, M. Quesada, G.B. Quinn, J.D. Westbrook, The RCSB Protein Data Bank: redesigned web site and web services, Nucleic acids research, 39 (2010) D392-D401.
29. R.H. Khan, M.K. Siddiqi, V.N. Uversky, P. Salahuddin, Molecular docking of Aβ1–40 peptide and its Iowa D23N mutant using small molecule inhibitors: Possible mechanisms of Aβ-peptide inhibition, International journal of biological macromolecules, 127 (2019) 250-270.
30. J. Bieschke, M. Herbst, T. Wiglenda, R.P. Friedrich, A. Boeddrich, F. Schiele, D. Kleckers, J.M. Lopez del Amo, B.A. Grüning, Q. Wang, Small-molecule conversion of toxic oligomers to nontoxic β-sheet–rich amyloid fibrils, Nature chemical biology, 8 (2012) 93-101.
31. T. Rom, N. Kumar, A. Agrawal, A. Gaur, A.K. Paul, Syntheses, crystal structures, topology and dual electronic behaviors of a family of amine-templated three-dimensional zinc-organophosphonate hybrid solids, Journal of Molecular Structure, 1263 (2022) 133087.

32. L. Krause, R. Herbst-Irmer, G.M. Sheldrick, D. Stalke, Comparison of silver and molybdenum microfocus X-ray sources for single-crystal structure determination, Journal of applied crystallography, 48 (2015) 3-10.
33. G.M. Sheldrick, Crystal structure refinement with SHELXL, Acta Crystallographica Section C: Structural Chemistry, 71 (2015) 3-8.
34. I.Y. Zhang, J. Wu, X. Xu, Extending the reliability and applicability of B3LYP, Chemical Communications, 46 (2010) 3057-3070.
35. T. Vishwanath, A. Ashish, C.R. Shankar, K. Amar, Single-crystal XRD, Hirshfeld surfaces, 3D energy framework calculations, and DFT studies of 4, 5-diphenyl-1, 3, 4-thiadiazole-2-thiolate: a mesoionic compound, Journal of Molecular Structure, (2022) 133290.
36. M. Ashfaq, A. Ali, M.N. Tahir, A. Kuznetsov, K.S. Munawar, S. Muhammad, Synthesis, single-crystal exploration, hirshfeld surface analysis, and DFT investigation of the thiosemicarbazones, Journal of Molecular Structure, 1262 (2022) 133088.
37. E. Torres, G.A. DiLabio, A (nearly) universally applicable method for modeling noncovalent interactions using B3LYP, The Journal of Physical Chemistry Letters, 3 (2012) 1738-1744.
38. M.P. Andersson, P. Uvdal, New scale factors for harmonic vibrational frequencies using the B3LYP density functional method with the triple-ζ basis set 6-311+ G (d, p), The Journal of Physical Chemistry A, 109 (2005) 2937-2941.
39. A. Costa Jr, G. Ondar, O. Versiane, J. Ramos, T. Santos, A. Martin, L. Raniero, G. Bussi, C.T. Soto, DFT: B3LYP/6-311G (d, p) vibrational analysis of bis-(diethyldithiocarbamate) zinc (II) and natural bond orbitals, Spectrochimica Acta Part A: Molecular and Biomolecular Spectroscopy, 105 (2013) 251-258.
40. A. Bayrakdar, S. Mert, R. Kasımoğulları, S. Bangaru, P. Manivannan, Synthesis, spectroscopic (FT-IR and NMR), DFT and molecular docking studies of ethyl 1-(3-nitrophenyl)-5-phenyl-3-((4-(trifluoromethyl) phenyl) carbamoyl)-1H-pyrazole-4-carboxylate, Research on Chemical Intermediates, 48 (2022) 2087-2109.
41. A. Fatima, G. Khanum, A. Sharma, N. Siddiqui, S. Muthu, R.J. Butcher, S.K. Srivastava, S. Javed, Synthesis, single crystal X-ray, DFT, Hirshfeld surface and molecular docking studies of 9-(2,4-dichlorophenyl)-4a-hydroxy-tetramethyl-octahydro-1H-xanthene-1,8(2H)-dione, Journal of Molecular Structure, 1268 (2022) 133613.

42. D. Seeliger, B.L. de Groot, Ligand docking and binding site analysis with PyMOL and Autodock/Vina, Journal of computer-aided molecular design, 24 (2010) 417-422.
43. B.L. Jejurikar, S.H. Rohane, Drug designing in discovery studio, Asian J. Res. Chem, 14 (2021) 135-138.
44. B. Das, A.T. Mathew, A.T. Baidya, B. Devi, R.R. Salmon, R. Kumar, Artificial intelligence assisted identification of potential tau aggregation inhibitors: ligand-and structure-based virtual screening, in silico ADME, and molecular dynamics study, Molecular Diversity, (2023) 1-19.
45. A.T. Baidya, B. Das, B. Devi, B. Långström, H. Ågren, T. Darreh-Shori, R. Kumar, Mechanistic insight into the inhibition of choline acetyltransferase by proton pump inhibitors, ACS Chemical Neuroscience, 14 (2023) 749-765.
46. R. Kumar, A. Nordberg, T. Darreh-Shori, Amyloid-β peptides act as allosteric modulators of cholinergic signalling through formation of soluble BAβACs, Brain, 139 (2016) 174-192.
47. T. Mosmann, Rapid colorimetric assay for cellular growth and survival: application to proliferation and cytotoxicity assays, Journal of immunological methods, 65 (1983) 55-63.